Reactions of Carbonyl Oxide with Aldehydes: Accurate Electronic Structure Methods, Kinetic Insights, and Atmospheric Implications

Chaolu Xie[1] Bo Long*[1,2]

[1] College of Physics and Mechatronic Engineering, Guizhou Minzu University, Guiyang 550025, China.
[2]College of Materials Science and Engineering, Guizhou Minzu University, Guiyang 550025, China

Correspondence to: Bo Long (wwwltcommon@sina.com)

Abstract: Carbonyl oxide (CH_2OO) is paramount in atmospheric oxidation chemistry, yet quantitative kinetics data for its bimolecular reactions are very limited and even unknown. Here we establish a computational framework to obtain quantitative kinetics from small to large reaction systems. For CH_2OO + HCHO, we develop electronic structure methods to reach CCSDTQ/CBS accuracy for its activation enthalpies at 0 K. For CH_2OO + aldehydes (RCHO; R = CH_3-C_5H_{11}, CH_2F, CHF_2, CF_3), we introduce two strategies that recover CCSDTQ/CBS-quality activation enthalpies at 0 K. A dual-level strategy has been used to calculate their kinetics. The calculated rate constants show excellent agreement with available experimental data for CH_2OO + RCHO (R = CH_3–C_3H_7), which validates the designed computational framework. We find that fluorination leads to exceptional rate enhancement, with reactions of CHF_2CHO and CF_3CHO exceeding 10^{-10} cm^3 $molecule^{-1}$ s^{-1} over 200–320 K, approaching the collision limit. We also find that fluorination-driven reactivity enhancement originates predominantly from lower-level electronic effects than that of post-CCSD(T). Incorporation of the kinetics into a global chemical transport model uncovers previously unrecognized atmospheric impacts, with CH_2OO + HCHO reducing nighttime CH_2OO and gas-phase sulfate concentrations by 25.3% in Antarctica and 12.2% over Canada, respectively. The present findings address a long-term challenge in how to obtain quantitative kinetics for large molecular systems, where post-CCSD(T) calculations are prohibitive and provide new insights into the chemical transformation of CH_2OO and fluorinated aldehydes in the atmosphere.

*Corresponding author, E-mail: wwwltcommon@sina.com (Bo Long)

1 Introduction

Aldehydes are a major class of oxygenated volatile organic compounds (OVOCs) that substantially influence atmospheric oxidative capacity, secondary organic aerosol (SOA) formation, and air quality (Lary and Shallcross, 2000; Liu et al., 2022; Zhao et al., 2024; Li et al., 2024; Mellouki et al., 2015; Bao et al., 2025; Zhang et al., 2012; Bari and Kindzierski, 2018; Edwards et al., 2014; Yang et al., 2018). They originate from both direct emissions—including biomass and fossil-fuel combustion, biogenic sources, and vehicle exhaust—and secondary production via VOC oxidation (Zhao et al., 2024; Knote et al., 2014; Parrish et al., 2012; Chen et al., 2014; Luecken et al., 2012; Grosjean et al., 1983). Their atmospheric removal is governed primarily by photolysis and OH reactions during daytime, whereas fluorinated aldehydes exhibit notably reduced OH reactivity (Wenger, 2006; Jiménez et al., 2007; Atkinson and Pitts, 1978; Lily et al., 2021; Sellevåg et al., 2005; Scollard et al., 1993; Thévenet et al., 2000; D'anna et al., 2001). NO_3 reactions constitute a nighttime sink but proceed extremely slow, highlighting the need to identify alternative nocturnal loss pathways (Cabañas et al., 2001; Bossmeyer et al., 2006; Papagni et al., 2000).

Stabilized Criegee intermediates (sCIs), key intermediate species of O_3-initiated alkene ozonolysis (Criegee, 1975; Criegee and Wenner, 1949), play critical roles in atmospheric oxidation and SOA formation (Khan et al., 2018; Novelli et al., 2014; Percival et al., 2013; Chhantyal-Pun et al., 2020) and react rapidly with acids (Cabezas and Endo, 2019; Chung et al., 2019; Peltola et al., 2020; Foreman et al., 2016; Raghunath et al., 2017), amides (Wei et al., 2022; Long et al., 2025), and SO_2 (Berndt et al., 2014; Boy et al., 2013; Manonmani et al., 2023; Kukui et al., 2021). Accurate kinetics for their bimolecular reactions are therefore essential for constraining their atmospheric fate.

Table 1. Rate constants of CH_2OO + HCHO by previous investigation at different temperatures and pressures.

Reaction	P (Torr)	T (K)	k(T) (cm^3 $molecule^{-1}$ s^{-1})	Ref.
Exp.	56	296	$(4.11 \pm 0.25) \times 10^{-12}$	(Luo et al., 2023)
	78	275	$(4.84 \pm 0.41) \times 10^{-12}$	(Enders et al., 2024)
		295	$(3.50 \pm 0.35) \times 10^{-12}$	
Theory	10	213	3.28×10^{-9}	(Zhang et al., 2023)
	202	230	1.29×10^{-9}	
	406	259	3.52×10^{-10}	
	760	296	5.51×10^{-10}	
		295	5.71×10^{-10}	
		296	6.52×10^{-11}	(Long et al., 2021)
		275	1.11×10^{-10}	
		295	6.68×10^{-11}	
		296	3.01×10^{-11}	This work
		275	5.62×10^{-11}	
		295	3.10×10^{-11}	

Despite numerous studies on CH_2OO + aldehydes, important gaps remain (Table 1 and Figure 1) for CH_2OO + HCHO, theoretical and experimental rate constants differ by an order of magnitude (Luo et al., 2023; Enders et al., 2024; Long et al., 2021; Zhang et al., 2023); prior work on CH_2OO + CH_3CHO/C_2H_5CHO/C_3H_7CHO (Tables 2-3) relied primarily on CCSD(T) despite evidence that higher-level excitations are required (Taatjes et al., 2012; Elsamra et al., 2016; Stone et al., 2014; Berndt et al., 2015; Jiang et al., 2024; Kaipara and Rajakumar, 2018; Liu et al., 2020; Liu et al., 2023; Cornwell et al., 2023; Debnath and Rajakumar, 2024); and key effects such as anharmonicity, torsional anharmonicity, and recrossing were generally neglected (Luo et al., 2023; Enders et al., 2024; Kaipara and Rajakumar, 2018; Debnath and Rajakumar, 2024; Jalan et al., 2013).

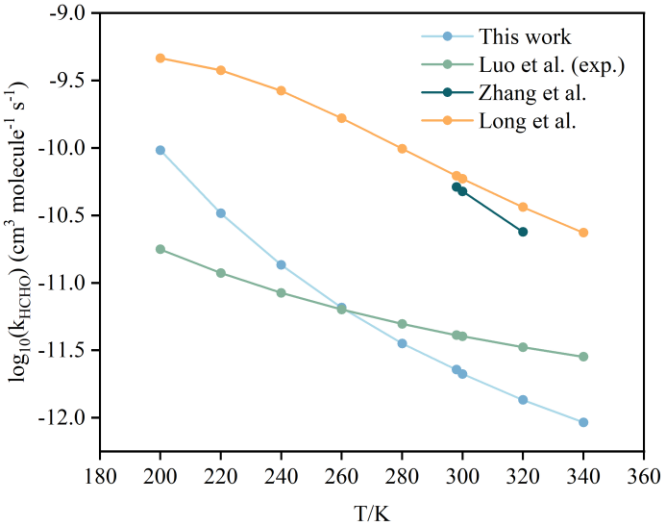

Figure 1. A comparison of reported rate constants for the CH_2OO + HCHO reaction from previous studies at different temperatures and high-pressure limit.

Table 2. Rate constants of CH_2OO + CH_3CHO by previous investigation at different temperatures and pressures.

Reaction	P (Torr)	T (K)	k(T) (cm^3 $molecule^{-1}$ s^{-1})	Ref.
Exp.	4	293	$(9.50 \pm 0.70) \times 10^{-13}$	(Taatjes et al., 2012)
	25	298	$(1.20 \pm 0.20) \times 10^{-12}$	(Elsamra et al., 2016)
		340	$(8.00 \pm 1.10) \times 10^{-13}$	
	4	298	$(1.10 \pm 0.10) \times 10^{-12}$	
	50		$(1.30 \pm 0.20) \times 10^{-12}$	
	25	295	$(1.48 \pm 0.04) \times 10^{-12}$	(Stone et al., 2014)
	760	297	$(1.70 \pm 0.50) \times 10^{-12}$	(Berndt et al., 2015)
	78	275	$(2.37 \pm 0.21) \times 10^{-12}$	(Enders et al., 2024)
		295	$(1.61 \pm 0.14) \times 10^{-12}$	
	50	280	$(2.57 \pm 0.46) \times 10^{-12}$	(Jiang et al., 2024)
		298	$(2.13 \pm 0.38) \times 10^{-12}$	
	5.5	298	$(1.73 \pm 0.32) \times 10^{-12}$	
	10		$(2.08\pm 0.38) \times 10^{-12}$	
	30		$(2.10\pm 0.38) \times 10^{-12}$	
	50		$(2.13\pm 0.38) \times 10^{-12}$	
	100		$(2.16 \pm 0.38) \times 10^{-12}$	
	80	275	$(10.20 \pm 0.80) \times 10^{-13}$	(Cornwell et al., 2023)

		295	$(8.00 \pm 0.70) \times 10^{-13}$	
Theory	760	275	4.63×10^{-12}	This work
		280	4.02×10^{-12}	
		293	2.83×10^{-12}	
		295	2.69×10^{-12}	
		297	2.56×10^{-12}	
		298	2.50×10^{-12}	

Moreover, no kinetic data exist for reactions with larger or fluorinated aldehydes, including pentanal, hexanal, CH_2FCHO, CHF_2CHO, and CF_3CHO. To address these gaps, atmospheric models have effectively utilized rate constants derived from empirical structure–reactivity relationships (SRRs)—such as those proposed by Jenkin et al. (Jenkin et al., 2018)—which provide a practical and robust framework for large-scale modeling. Given the inherent complexity of computing atmospheric kinetics, these empirical methods remain a primary tool for estimation.

Table 3. Rate constants of CH_2OO + RCHO (R = C_2H_5/C_3H_7) by previous investigation at different temperatures and pressures.

Reaction		P	T	*k(T)* (cm^3 $molecule^{-1}$ s^{-1})	Ref.
C_2H_5CHO	Exp.	50 Torr	283 K	$(3.55 \pm 0.50) \times 10^{-12}$	(Liu et al., 2020)
			298 K	$(3.12 \pm 0.44) \times 10^{-12}$	
		5 Torr	298 K	$(2.39 \pm 0.22) \times 10^{-12}$	
		5.2 Torr		$(2.52 \pm 0.24) \times 10^{-12}$	
		10 Torr		$(3.07 \pm 0.20) \times 10^{-12}$	
		25 Torr		$(2.12 \pm 0.19) \times 10^{-12}$	
		75 Torr		$(3.30 \pm 0.20) \times 10^{-12}$	
		100 Torr		$(3.08 \pm 0.19) \times 10^{-12}$	
		150 Torr		$(3.18 \pm 0.19) \times 10^{-12}$	
		200 Torr		$(3.19 \pm 0.21) \times 10^{-12}$	
		78 Torr	275 K	$(4.35 \pm 0.38) \times 10^{-12}$	(Enders et al., 2024)
			295 K	$(3.29 \pm 0.29) \times 10^{-12}$	
	Theory	HPL	283 K	2.29×10^{-12}	(Kaipara and Rajakumar, 2018)
			298 K	1.51×10^{-12}	
			275 K	2.92×10^{-12}	
			295 K	1.63×10^{-12}	
			283 K	4.49×10^{-12}	This work
			298 K	3.11×10^{-12}	

			275 K	5.57×10^{-12}	
			295 K	3.33×10^{-12}	
C_3H_7CHO	Exp.	50 Torr	253 K	$(4.20 \pm 0.10) \times 10^{-12}$	(Debnath and Rajakumar, 2024)
			268 K	$(3.61 \pm 0.10) \times 10^{-12}$	
			283 K	$(2.99 \pm 0.22) \times 10^{-12}$	
			298 K	$(2.63 \pm 0.14) \times 10^{-12}$	
	Theory	HPL	253 K	8.83×10^{-12}	This work
			268 K	5.30×10^{-12}	
			283 K	3.38×10^{-12}	
			298 K	2.27×10^{-12}	

Here, we investigate CH_2OO reactions with nine aldehydes (RCHO; R = H, CH_3, C_2H_5, C_3H_7, C_4H_9, C_5H_{11}, CH_2F, CHF_2, CF_3) to obtain quantitative rate constants and to establish a general high-accuracy computational protocol applicable from small benchmark systems to large atmospheric molecules. For the prototypical CH_2OO + HCHO reaction, we develop the GMM(Q).L4 composite scheme that approaches full-CI accuracy, and for the broader reaction suite we devise a scalable strategy capable of delivering near–full-CI activation energies. Dual-level strategy calculations accounting for all major anharmonic and dynamical effects yield benchmark-quality rate constants, which are subsequently implemented in GEOS-Chem to quantify their atmospheric impacts. This work provides a broadly extensible computational framework and significantly advances the understanding of CH_2OO–aldehyde chemistry.

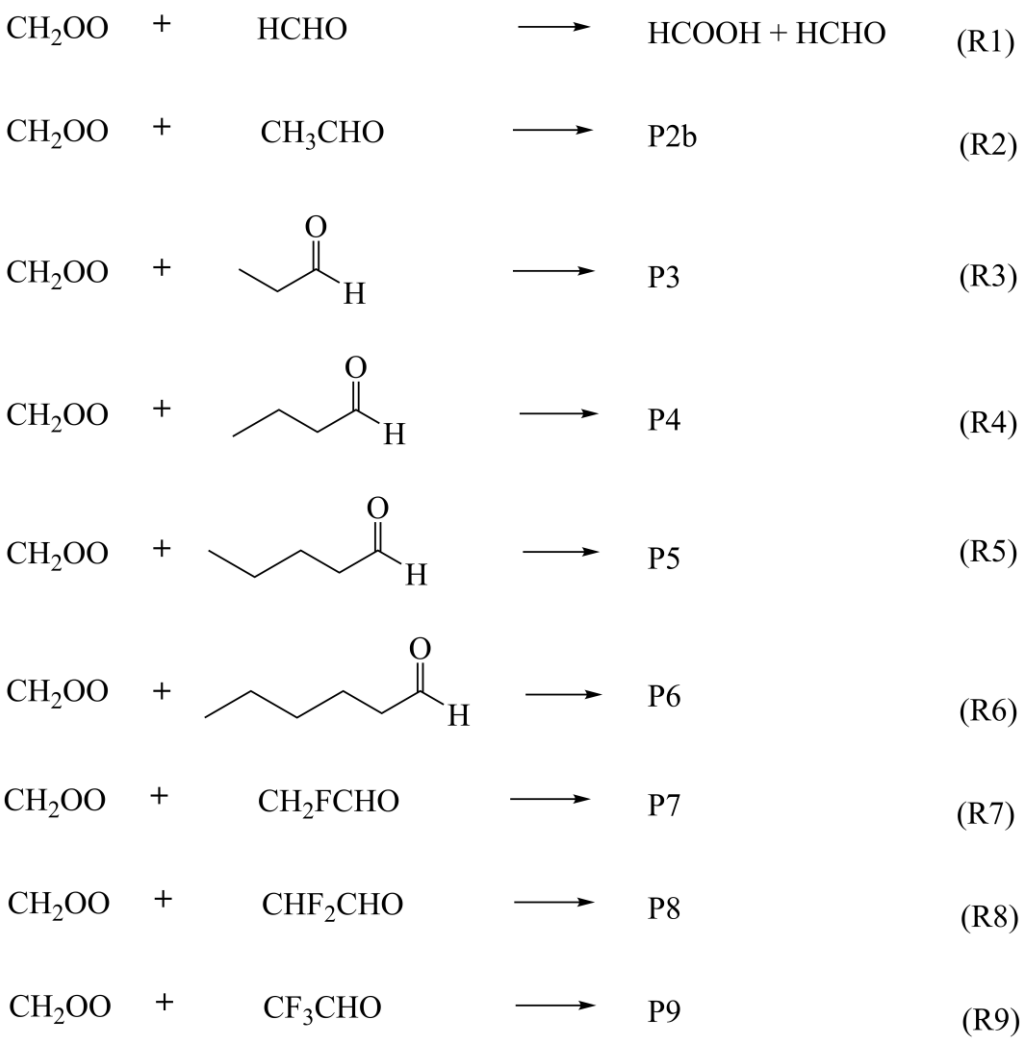

Scheme 1. Reactions of CH_2OO with aldehydes

2 Computational methods and strategies

2.1 Electronic structure best estimates for the CH_2OO + HCHO reaction

Accurate electronic-structure data are essential for quantitative kinetics. All geometries and harmonic frequencies were optimized at the CCSD(T)-F12a/cc-pVTZ-F12 level (Adler et al., 2007; Knizia et al., 2009; Bischoff et al., 2009). To approach the full-CI limit for single-point energies, we developed a composite protocol, GMMQ.L4, which effectively reproduces

CCSDTQ/CBS quality:

$$E_{\mathrm{GMMQ.L4}} = E_{\mathrm{MW2-F12.L}} + \Delta E_{\mathrm{T-(T)}} + \Delta E_{\mathrm{(Q)-T}} + \Delta E_{\mathrm{Q-(Q)}} \quad (1)$$

Here, $E_{\mathrm{MW2-F12.L}}$ is obtained from the previously validated MW2-F12.L scheme which detailed in Table S7 (Long et al., 2021). $\Delta E_{\mathrm{T-(T)}}$ (CCSDT–CCSD(T)) and $\Delta E_{\mathrm{(Q)-T}}$ (CCSDT(Q)–CCSDT) are extrapolated to the CBS limit (cc-pVDZ → cc-pVTZ and cc-pVDZ → VTZ(d)) using

$$\Delta E_{\mathrm{L}} = \Delta E_{\mathrm{CBS}} + \frac{\mathrm{A}}{\mathrm{L}^3} \quad (2)$$

with L=2 for cc-pVDZ and 3 for cc-pVTZ and VTZ(d).

The final correction, $\Delta E_{\mathrm{Q-(Q)}}$, is evaluated at the CCSDTQ–CCSDT(Q) level using the VDZ(NP) basis set. VTZ(d) employs H(s) and heavy-atom(spd), while VDZ(NP) uses H(s) and heavy-atom(sp) functions (Chan and Radom, 2015).

Coupled-cluster theory converges systematically toward Full configuration interaction (Full-CI), but the steep scaling necessitates truncation. Previous studies have established rapid basis-set convergence for both CCSDT(Q)–CCSDT and CCSDT–CCSD(T) (Long et al., 2021; Long et al., 2019; Xia et al., 2025). Consistently, the CCSDTQ–CCSDT(Q) contribution in our system is only 0.096 kcal mol^{-1}, indicating that excitations beyond quadruples contribute <0.10 kcal mol^{-1} in Table S1. Thus, GMMQ.L4//CCSD(T)-F12a/cc-pVTZ-F12 serves as the benchmark level in our dual-level kinetics framework.

We further compared GMMQ.L4 with the W3X-L composite method (Chan and Radom, 2015) for reaction R1. Although both protocols include identical post-CCSD(T) contributions, GMMQ.L4 employs the MW2-F12.L component, whereas W3X-L is based on W2X. Detailed comparisons are provided in Tables S1, S7, and S8. The observed deviation of 0.24 kcal mol^{-1} indicates that W3X-L does not achieve quantitatively reliable barrier heights for this system. Our analysis shows that this discrepancy primarily originates from the difference between MW2-F12.L and W2X. Specifically, MW2-F12.L includes HF energies, ΔCCSD and Δ(T) correlation contributions, core–valence (Δ(C+V)) corrections, and scalar relativistic (Δ(C+R)) effects, all evaluated with larger basis sets. In contrast, W2X comprises analogous HF, ΔCCSD, Δ(T), and Δ(C+R) terms, but these are computed using smaller basis sets. The calculated results the difference of 0.24 kcal mol^{-1} comes from the Δ(C+V) and Δ(C+R) terms, which differ by 0.19 kcal/mol and 0.12 kcal/mol, respectively. Additionally, CCSD(T)-F12 convergence

was verified by comparing W2X energies computed with cc-pVTZ-F12 and cc-pVDZ-F12 geometries; the difference of only 0.04 kcal mol^{-1} confirms near-CBS performance of CCSD(T)-F12 for structural and vibrational data (See Table 4).

Table 4. Calculated enthalpies of activation at 0 K ($\Delta H_0^{\ddagger}$ in kcal/mol, relative to the bimolecular reactants) and unsigned deviation (MUD) (in kcal/mol).

Methods	$\Delta H_0^{\ddagger}$	
	TS1	UD
GMMQ.L4//CCSD(T)-F12a/cc-pVTZ-F12	−4.97	0.00
BE1//CCSD(T)-F12a/cc-pVTZ-F12	−4.97	0.00
BE2//CCSD(T)-F12a/cc-pVTZ-F12	−4.97	0.00
M11-L/MG3S	−5.16	0.19
W3X-L//CCSD(T)-F12a/cc-pVTZ-F12	−5.22	0.24
MW2-F12.L//CCSD(T)-F12a/cc-pVTZ-F12	−5.41	0.44
W2X//DF-CCSD(T)-F12a/jun-cc-pVDZ	−5.60	0.63
W2X//CCSD(T)-F12a/cc-pVTZ-F12	−5.62	0.64
W2X//CCSD(T)-F12a/cc-pVDZ-F12	−5.66	0.68
W2X//DF-CCSD(T)-F12b/VDZ(d)	−5.66	0.68
W2X//DF-CCSD(T)-F12a/cc-pVDZ	−5.72	0.74
W2X//DF-CCSD(T)-F12b/VDZ(NP)	−6.19	1.22

2.2 Electronic structure best estimates for R2-R9

Geometrical optimization and frequency calculations. Reliable optimized geometries and harmonic frequencies are essential for obtaining quantitative 0 K activation enthalpies. For reaction R1, we verified that CCSD(T)-F12a/cc-pVDZ-F12 delivers results essentially identical to CCSD(T)-F12a/cc-pVTZ-F12, allowing us to employ the lower-cost cc-pVDZ-F12 basis for reaction R2. However, for larger CH_2OO + aldehyde systems, CCSD(T)-F12a/cc-pVDZ-F12 remains computationally prohibitive. To overcome this limitation, we systematically benchmarked density-fitted F12 coupled-cluster methods (DF-CCSD(T)-F12b) (Győrffy and Werner, 2018) across a range of compact basis sets (Table 4). Remarkably, DF-CCSD(T)-F12b/jun-cc-pVDZ (Parker et al., 2014) and DF-CCSD(T)-F12b/VDZ(d) exhibit exceptionally small mean unsigned deviations of only 0.03 and 0.04 kcal mol^{-1}, respectively, relative to the Best Estimate for W2X reference (Table S2).This identifies a new, computationally efficient F12 protocol capable of retaining sub-0.05 kcal mol^{-1} accuracy for CH_2OO–

aldehyde reactions, representing a key methodological advance enabling routine treatment of larger Criegee intermediate–carbonyl systems. Accordingly, we employed DF-CCSD(T)-F12b/jun-cc-pVDZ for R3–R5 and R7–R8, and DF-CCSD(T)-F12b/VDZ(d) for R3–R6 to obtain geometries and vibrational frequencies with near-CBS accuracy at greatly reduced cost.

Single point energy calculations. To further reduce the cost of CCSDTQ/CBS-quality calculations, we developed a new composite scheme, denoted BE1, which achieves near-GMMQ.L4 accuracy. The BE1 single-point energy is defined as

$$E_{\mathrm{BE1}} = E_{\mathrm{W2X}} + \Delta E_{(Q)-(T)} + \Delta E_{\mathrm{SC1}} \qquad (3)$$

where $\Delta E_{(Q)-(T)}$ is the CCSDT(Q) – CCSD(T) correction evaluated with the VDZ(NP) basis set for reactions R1–R8.

The term ΔE_{SC1} introduces a structure-specific correction and is given by

$$\Delta E_{\mathrm{SC1}} = E^{\mathrm{TS1}}_{\mathrm{GMMQ.L4}} - E^{\mathrm{TS1}}_{\mathrm{W2X}} - [E^{\mathrm{TS1}}_{\mathrm{CCSDT(Q)/VDZ(NP)}} - E^{\mathrm{TS1}}_{\mathrm{CCSD(T)/VDZ(NP)}}] \qquad (4)$$

This formulation anchors the composite energy to a single high-level reference transition state (TS1), ensuring the transferability of the correction across the reaction series. The value of ΔE_{SC1} is 0.04 kcal/mol.

For comparison, we also employed our previously reported strategy, BE2 (Sun et al., 2024), which augments the W2X energy with a constant post-CCSD(T) correction:

$$E_{\mathrm{BE2}} = E_{\mathrm{W2X}} + \Delta E_{\mathrm{SC2}} \qquad (5)$$

where ΔE_{SC2} is the GMMQ.L4 − W2X difference for TS1 (0.64 kcal mol^{-1} in Table 4).

Both BE1 and BE2 offer computationally inexpensive routes to emulate CCSDTQ/CBS performance by incorporating systematic, physically motivated corrections. In the present work, the BE1 protocol served as the high-level (HL) energy in our dual-level kinetics strategy, with the underlying structures obtained from

- BE1//CCSD(T)-F12a/cc-pVDZ-F12 for R2,
- BE1//DF-CCSD(T)-F12b/jun-cc-pVDZ for R3–R5 and R7–R8, and
- BE1//DF-CCSD(T)-F12b/VDZ(d) for R6.

This composite strategy enables sub-kcal mol^{-1} accuracy at a fraction of the cost of full GMMQ.L4 or CCSDTQ/CBS calculations.

2.3. Electronic structure density functional methods

To enable efficient direct kinetics calculations for the full aldehyde series, we systematically evaluated a range of density functional methods against the BE1 benchmark. Among all tested functionals, M11-L (Peverati and Truhlar, 2012)/MG3S (Lynch et al., 2003) exhibits the best performance, yielding a remarkably small mean unsigned deviation (MUD) of 0.32 kcal mol^{-1} cross reactions R1–R8 (Figure 2). This accuracy—well within sub-kcal mol^{-1} agreement with the BE1 high-level reference—identifies M11-L/MG3S as a reliable and computationally economical low-level (LL) method for the dual-level kinetics framework. Accordingly, M11-L/MG3S was used for all direct kinetics calculations involving CH_2OO + aldehyde reactions. Standard vibrational scaling factors were applied as listed in Table S3.

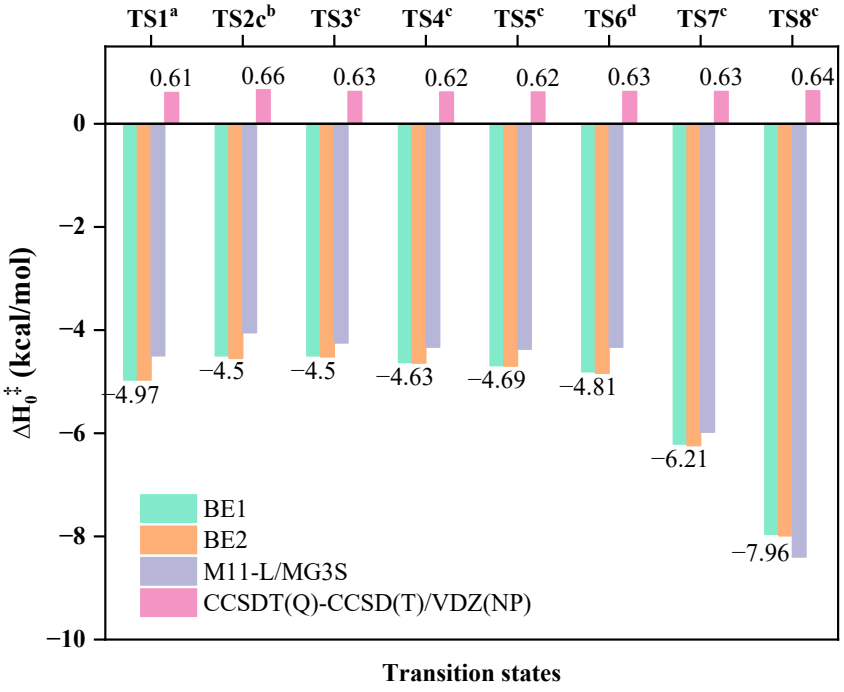

Figure 2. Best estimate for reaction R1-R8 at different level.

[a]The best estimate results by BE1//CCSD(T)-F12a/cc-pVTZ-F12 in the CH_2OO + HCHO reaction.

[b]The best estimate results by BE1//CCSD(T)-F12a/cc-pVDZ-F12 in the CH_2OO + CH_3CHO reaction.

[c]The best estimate results by BE1//DF-CCSD(T)-F12b/jun-cc-pVDZ in the CH_2OO + XCHO (X=C_2H_5/C_3H_7/C_4H_9/CH_2F/CHF_2) reaction.

[d]The best estimate results by BE1//DF-CCSD(T)-F12b/VDZ(d) in the CH_2OO + $C_5H_{11}CHO$ reaction.

Previous studies have suggested that standard scaling factors may be unsuitable for certain transition states, we explicitly

investigated the impact of anharmonicity. Using the method described by Long et al. (Long et al., 2023), we calculated specific scaling factors by (See Tables S4 and S5). However, we found that anharmonicity corrections to the zero-point energy (ZPE) were negligible. Consequently, standard scaling factors are employed throughout this work. Full methodological details are provided in the Supporting Information.

2.4. Kinetics Methods

High-pressure limited rate constants for R2-R6. Dual-level strategy (Long et al., 2019; Sun et al., 2024; Long et al., 2016) was employed, in which high-level (HL) conventional transition state theory (TST) provides the baseline rate constants, whereas canonical variational transition state theory with small-curvature tunneling (CVT/SCT) at the low-level (LL) supplies kinetic corrections. The high-pressure-limit rate constants were obtained according to eq 5:

$$k = k_{\mathrm{HL}}^{\mathrm{TST}}(T)\kappa_{\mathrm{LL}}(\mathrm{T})\Gamma_{\mathrm{LL}}(T)F_{\mathrm{fwd}}^{\mathrm{MS-T,LL}}(\mathrm{T}) \qquad (5)$$

where $k_{\mathrm{HL}}^{\mathrm{TST}}$ is the rate constants calculated at HL. $\kappa_{\mathrm{LL}}(T)$ and $\Gamma_{\mathrm{LL}}(T)$ is tunneling and recrossing transmission coefficients calculated at the LL level. $\mathrm{F}_{\mathrm{fwd}}^{\mathrm{MS-T,LL}}(\mathrm{T})$ is referred to multi-structural anharmonic factor calculated by eqn (6) at the M11-L/MG3S level

$$\mathrm{F}_{\mathrm{fwd}}^{\mathrm{MS-T,LL}} = \frac{\mathrm{F}_{\mathrm{TS}}^{\mathrm{MS-T}}}{\mathrm{F}_{\mathrm{R}}^{\mathrm{MS-T}}} \qquad (6)$$

High-pressure limited rate constants for R1 and R7-R9. The rate constants of R1 and R7-R9 were calculated by simultaneously considering both the loose transition state between reactants and the van der Waals complex, and the tight TS between reactants and products. The rate constant for the loose TS (k_{loose}) was calculated using variable-reaction-coordinate variational transition-state theory (VRC-VTST) (Georgievskii and Klippenstein, 2003; Zheng et al., 2008; Bao et al., 2016b) with 500 configurations for Monte Carlo sampling. A single-faceted dividing surface was constructed with two pivot points, following procedures validated in previous work (Long et al., 2021). One pivot point was placed along a vector at a distance *d* from the center of mass (COM) of CH_2OO, oriented perpendicular to the CH_2OO plane, while the other was placed similarly with respect to CH_2F/CHF_2/CF_3CHO. The pivot distance was set to *d*=0.05 Å. The reaction coordinate *s* was defined as the separation between the two pivot points, ranging from 3.5 to 10 Å for R7, 3.9 to 10 Å for R8, 4.4 to 10 Å for R9 with increments

of 0.1 Å. The rate constant for the tight TS (k_{tight}) was calculated by using dual-level strategy presented above. The overall rate constant was then obtained using the steady-state approximation (Garrett and Truhlar, 1982; Zhang et al., 2020; Long et al., 2024) in equation (7).

$$k = \frac{k_{\mathrm{loose}} k_{\mathrm{tight}}}{k_{\mathrm{loose}} + k_{\mathrm{tight}}} \quad (7)$$

Pressure-dependent rate constant. Master equation method with Rice−Ramsperger−Kassel−Marcus theory (ME/RRKM) (Kenneth A. Holbrook, 1996; Fernández-Ramos et al., 2006; Georgievskii et al., 2013; Klippenstein, 2003) was used to calculate pressure dependence of rate constants for the reactions of CH_2OO with HCHO and CH_3CHO. The calculation utilized parameters from W3X-L//CCSD(T)-F12a/cc-pVTZ-F12 for reaction R1 and W2X//DF-CCSD(T)-F12b/jun-cc-pVDZ for reaction R2. Both reactions were modeled with N_2 as the bath gas, employing Lennard-Jones parameters from Table S6 and an average energy transfer parameter of $\langle\Delta E\rangle_{\mathrm{down}}$ = 200 cm^{-1}. Within this framework, the pressure effect was approximated as the quotient of the high-pressure limit and a pressure ratio. This ratio is defined as the value at 7.5 × 10^3 Torr relative to its value at different pressures. We further inspection the simplification of reaction R2 in Scheme 2. The kinetic results for Schemes 2a and 2b demonstrate remarkable robustness, with the simplification introducing no statistically significant perturbations to the calculated rate constants.

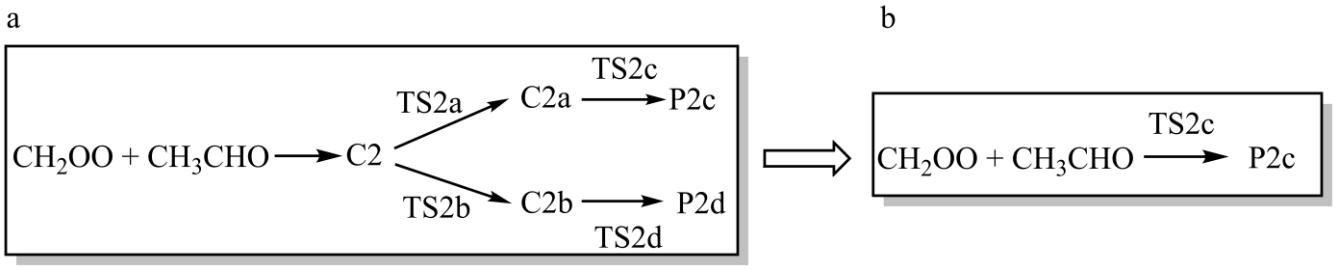

Scheme 2. The reaction mechanism for the CH_2OO + CH_3CHO reaction.

2.5. Atmospheric modeling

We performed two atmospheric simulations included reaction R1 and R2 to investigate the significance of these reactions by observing the change of concentration globally in GEOS-Chem. This included: (1) a “base” model using default setting (2) a “update1” model adding a new sink of HCHO in the base model, (3) a “update2” model adding a new sink of CH_3CHO in

the base model. These models include the meteorological data observations assimilated from the NASA Modern-Era Retrospective Analysis for Research and Applications (MERRA-2) (Gelaro et al., 2017) and Emissions data from the default Harmonized Emission Component (HEMCO) (Lin et al., 2021). For anthropogenic emissions, we used the Community Emissions Data System (CEDS) (Hoesly et al., 2018). For biogenic emissions, we used offline VOC emissions computed from the Model of Emissions of Gases and Aerosols from Nature (MEGAN) (Guenther et al., 2012). The simulation was carried out with 2° × 2.5° horizontal resolution at 47 vertical layers. The annual changes displayed are obtained from simulations that employed meteorological data from February 1, 2018, to January 31, 2019, following a six-month model spin-up.

2.6. Software.

Density functional calculations were performed by using the Gaussian 16 (Frisch et al., 2016). The coupled cluster calculations were performed by using the Molpro 2019 (Werner, 2019) and MRCC codes (Kállay et al., 2020). Multi-structural anharmonic calculations were performed in MSTor codes (Zheng et al., 2012). Rate constants were calculated using the Polyrate 2017-C (Zheng et al., 2017b), Gaussrate 2017-B codes (Zheng et al., 2017a), and KiSThlP 2021 (Canneaux et al., 2014). The master equation calculations were performed by utilizing the TUMME program (Zhang et al., 2022). Atmospheric modeling was performed by using GEOS-Chem 14.4.2 (Bey et al., 2001, (http://www.geos-chem.org, last access: 4 November 2025).

3. RESULTS AND DISSCUSSION

The enthalpy of activation at 0 K ($\Delta H_0^{\ddagger}$) is referred to the relative energies with zero-point energy between transition states and reactants.

3.1 The electronic structure of CH_2OO + HCHO

The reaction mechanism examined here is consistent with that established in earlier studies (Luo et al., 2023; Long et al., 2021; Jalan et al., 2013; Wang et al., 2022). The relative enthalpy profile for the CH_2OO + HCHO reaction is depicted in Figure 3, and the key data are summarized in Table 4. Notably, the activation enthalpy at 0 K obtained at the GMMQ.L4//CCSD(T)-

F12a/cc-pVTZ-F12 level (−4.97 kcal mol⁻¹) differs from that predicted by W3X-L//CCSD(T)-F12a/cc-pVTZ-F12 (−5.21 kcal mol⁻¹ in Table 4) and deviates even more substantially from the RCCSD(T)-F12a/VTZ-F12//B3LYP/MG3S value (−6.30 kcal mol⁻¹) (Jalan et al., 2013). These differences demonstrate the strong sensitivity of $\Delta H_0^{\ddagger}$ to the underlying electronic-structure treatment, thereby directly influencing predicted rate constants.

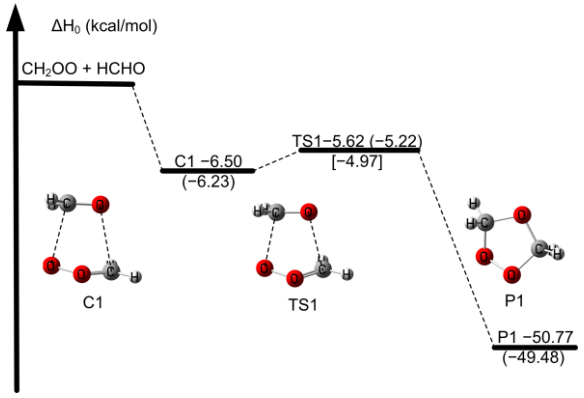

Figure 3. The relative enthalpies at 0 K for the reaction of CH_2OO + HCHO. Values are given for all species as calculated by W2X//CCSD(T)-F12a/cc-pVTZ-F12, and in parentheses and bracket, values are given for the transition state TS1 as calculated by W3X-L//CCSD(T)-F12a/cc-pVTZ-F12 and GMMQ.L4//CCSD(T)-F12a/cc-pVTZ-F12.

Previous studies have shown that post-CCSD(T) correlation is essential for quantitative barriers in Criegee chemistry (Long et al., 2021; Long et al., 2016; Xia et al., 2022). For TS1, the unsigned deviation between GMMQ.L4 and MW2-F12.L is 0.40 kcal mol⁻¹—slightly different with the ~0.50 kcal mol⁻¹ benchmark established for post-CCSD(T) effects (Long et al., 2021)—reaffirming the need for high-level correlation to achieve quantitative accuracy. We further find that the post-CCSD(T) contribution through CCSDT(Q), quantified by the W3X-L − W2X difference, is 0.44 kcal mol⁻¹, in excellent agreement with the 0.40 kcal mol⁻¹ value. This concordance highlights the robustness of W3X-L in capturing post-CCSD(T) contributions (Table 4). The remaining 0.24 kcal mol⁻¹ discrepancy between GMMQ.L4 and W3X-L primarily reflects differences between the MW2-F12.L and W2X components of TS1 (Tables S7 and S8). The 0.21 kcal mol⁻¹ deviation between MW2-F12.L and W2X further illustrates that larger basis sets are required for fully quantitative predictions.

This present work provides a rigorously benchmarked assessment of $\Delta H_0^{\ddagger}$ for the CH_2OO + HCHO reaction, explicitly quantifying post-CCSD(T) contributions and revealing their decisive role in achieving sub-kcal mol⁻¹ accuracy. The systematic comparison among GMMQ.L4, MW2-F12.L, and W3X-L underscores the reliability of our calculated results.

3.2. The electronic structure of $CH_2OO + CH_3CHO$

We aim to demonstrate the feasibility of simplifying the reaction mechanism of larger aldehydes with CH_2OO in Scheme 2. A partial reaction mechanism $CH_2OO + CH_3CHO$ has been reported in our previous work (Wang et al., 2022). We first consider the seven-membered ring pre-reaction complex C2 formation in Figure 4, which is consistent with our previous results (Wang et al., 2022). However, due to two distinct orientations of the methyl group in CH_3CHO toward CH_2OO, there are two rotation transition states TS2a and TS2b connecting C2 to the five-membered ring complexes C2a and C2b, respectively. Therefore, the process is only the transformation of complex in the reaction processes. Then, C2a and C2b undergo the corresponding transition state TS2c and TS2d responsible for the formation of P2a and P2b. The mechanism was depicted in Scheme 2a. However, the enthalpies of activation at 0 K for TS2a and TS2b are lower than those of TS2c and TS2d by 0.64 kcal/mol and 0.37 kcal/mol at W3X-L//CCSD(T)-F12a/cc-pVDZ-F12 in Figure 4, respectively. Therefore, TS2a and TS2b could be neglected from energetic point of view. We will also discuss it from the kinetics point of view.

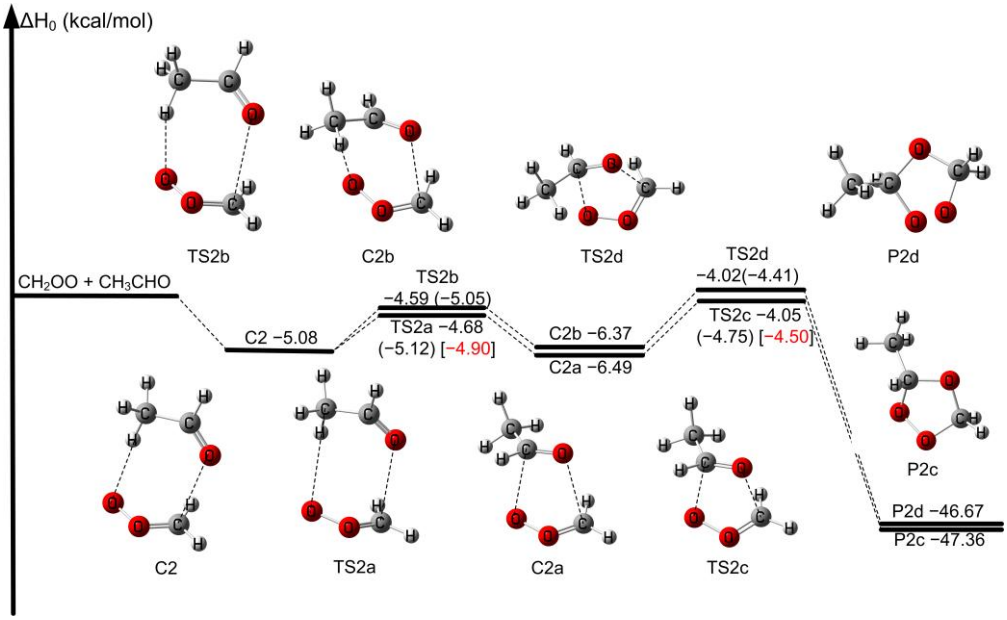

Figure 4. The relative enthalpies at 0 K for the reaction of $CH_2OO + CH_3CHO$. Values are given for all species as calculated by M11-L/MG3S, and in parentheses and bracket, values are given for the transition states as calculated by W3X-L//CCSD(T)-F12a/cc-pVDZ-F12 and BE1//CCSD(T)-F12a/cc-pVDZ-F12.

The five-membered ring complexes C2a and C2b can interconvert via $TS2_{ISO}$ with C=O bond rotation, which lies 2.51

kcal mol⁻¹ above C2a at the M11-L/MG3S level (Figure S4), similar to the reaction between CH_2OO and FCHO (Xia et al., 2024). For aldehydes with longer chains, the corresponding isomerization transition states of the five-membered ring complexes (Figures S5–S6) exhibit similarly low barriers, indicating facile interconversion, which also verified from kinetics perspective. Consequently, the complex mechanism can be effectively reduced to the straightforward reaction pathway b depicted in Scheme 2. Accordingly, the mechanism for CH_2OO with larger aldehydes was simplified to consider only the lowest-energy pathway corrected by torsional anharmonicity in kinetics calculations.

The $\Delta H_0^{\ddagger}$ for TS2c is −4.50 kcal mol⁻¹ at the BE1//CCSD(T)-F12a/cc-pVDZ-F12 level (See Table S9), which is 0.8 kcal mol⁻¹ higher than the result reported by Jalan et al. at the RCCSD(T)-F12a/VTZ-F12//B3LYP/MG3S level and 0.19 kcal mol⁻¹ higher than that of Wang et al at the WMS//M11-L/MG3S level (Wang et al., 2022; Jalan et al., 2013). BE1 and BE2 for TS2c agree well with each other in Figure 2 and Table S9, not only demonstrating the reliability of the computational protocol, but also capturing the essential physical origin underlying the quantitative description of $\Delta H_0^{\ddagger}$. The M11-L/MG3S has been chosen for direct dynamics calculations due to the MUD of 0.81 kcal mol⁻¹ in Table S9.

The validity of the DF-CCSD(T)-F12/jun-cc-pVDZ and DF-CCSD(T)-F12b/VDZ(d) methods was also confirmed for reaction R2. As shown in Table S9, these methods yielded mean unsigned deviations (MUD) of 0.05 and 0.02 kcal mol⁻¹, respectively, relative to the CCSD(T)-F12a/cc-pVDZ-F12 benchmark.

3.3. Electronic structure of CH_2OO + RCHO (R = C_2H_5/C_3H_7/C_4H_9/C_5H_{11})

The complexity of reactions R3–R6 increases with reactant system size owing to the presence of multiple conformers of both reactants and transition states (Table S10). Conformers for each reactant and transition state were obtained by rotating the dihedral angles listed in Table S10. Specifically, two conformers were identified for C_2H_5CHO, four for C_3H_7CHO, twelve for C_4H_9CHO, and thirty-five for $C_5H_{11}CHO$, arising from C–C bond rotations. In contrast, conformational diversity is even more pronounced for the transition states, with three conformers for TS3, eighteen for TS4, twenty-four for TS5, and seventy-nine for TS6, primarily due to internal C=O and C-C bond rotations.

As the carbon chain prolongs, the change in $\Delta H_0^{\ddagger}$ for R1-R6 is not obvious, but it presents a trend. We find a slight decrease in $\Delta H_0^{\ddagger}$ with the elongation of carbon chain for R2-R6 with the exception of R1. The $\Delta H_0^{\ddagger}$ calculated by best

estimate are −4.50, −4.50, −4.63, 4.69, and −4.81 kcal mol⁻¹ for R2-R6 (See Figure 2 and Table S11), which are about 3 kcal mol⁻¹ below the reaction of the corresponding reactants with HO_2 (Gao et al., 2024; Long et al., 2022; Ding and Long, 2022). Moreover, the influence of carbon chain length on enthalpy of activation for R2-R6 is analogue to the reaction of HO_2 and aldehydes (Gao et al., 2024). Also, BE1 and BE2 for TS2c–TS6 (Figure 2 and Table S11) exhibit excellent mutual consistency. This behavior can be attributed to the nearly invariant $(\mathrm{CCSDT(Q)} - \mathrm{CCSD(T)})/\mathrm{VDZ(NP)}$ term (~0.6 kcal mol⁻¹) among these transition states, demonstrating that the post-CCSD(T) contributions are almost uniform across this reaction series. These observations provide compelling evidence that both alkyl substitution and carbon-chain elongation negligibly modulate the magnitude of post-CCSD(T) corrections, implying that such higher-order correlation effects are intrinsically insensitive to substituent-induced electronic and conformational changes.

3.4. Electronic structure of CH_2OO + RCHO (R = CH_2F/CHF_2/CF_3)

The electronic structure information was depicted in Figure 2 and Table S12. The activation enthalpies at 0 K decrease significantly with the increasing number of fluorine substitutions in the methyl group of the aldehyde.

The $\Delta H_0^{\ddagger}$ for CH_2OO + CH_2FCHO (TS7) is −6.21 kcal mol⁻¹ by our best estimate, which is 1.31 kcal mol⁻¹ and 1.71 kcal mol⁻¹ lower than the reaction R1 and R2, respectively. Consequently, reaction R7 is expected to exhibit a significantly larger rate constant compared to the CH_2OO + HCHO/CH_3CHO reactions. This reduction in $\Delta H_0^{\ddagger}$ indicates that fluorine substitution enhances the reactivity of the aldehyde toward CH_2OO, which is similar to HO_2 + CF_3CHO (Long et al., 2022). For the reaction of CH_2OO + CHF_2CHO (R8), the $\Delta H_0^{\ddagger}$ is −7.96 kcal mol⁻¹, which is 1.75 kcal mol⁻¹ lower than that of the corresponding transition state, TS7. This value is close to that of CH_2OO + HCl (Foreman et al., 2016), which approaches the bimolecular collision limit, suggesting that the reaction R8 through the tight transition state is not the rate-determining step. Although fluorine substitution on the methyl group of the aldehyde leads to substantially enhanced reactivity toward CH_2OO, the post-CCSD(T) contributions from the $(\mathrm{CCSDT(Q)} - \mathrm{CCSD(T)})/\mathrm{VDZ(NP)}$ term (~0.6 kcal mol⁻¹) remain nearly identical across the transition states as shown in Figure 2, revealing that the higher-order correlation effects are largely insensitive to fluorination and establishing that the fluorination-driven reactivity enhancement originates primarily from lower-level electronic effects than that of post-CCSD(T).

Given the demonstrated accuracy of the M11-L/MG3S method for reactions R7 and R8, this method was subsequently applied to reaction R9, as depicted in Figure S3. Regarding CF_3CHO + CH_2OO (R9), the $\Delta H_0^{\ddagger}$ further decreases to −9.74 kcal/mol at M11-L/MG3S level. However, this value is slightly higher than the activation enthalpies observed for the universal mechanism of Criegee intermediates reacting with amides (Long et al., 2025), which are significantly submerged below the reactants by approximately 9 to 11 kcal/mol. This shows that this tight transition state is not the rate-determining step for reaction R9.

We further compare the calculated $\Delta H_0^{\ddagger}$ of the CH_2OO + RCHO (R = CH_2F, CHF_2, CF_3) reactions with those of the corresponding OH reactions. The $\Delta H_0^{\ddagger}$ for OH + CH_2FCHO is −1.15 kcal mol^{-1} at the CCSD(T)//M06-2X/aug-cc-pVTZ level, which is 5.06 kcal mol^{-1} higher than that of R7. We also find that the $\Delta H_0^{\ddagger}$ for R8 by our best estimate is 8.19 kcal mol^{-1} lower than that of OH + CHF_2CHO, calculated at the CCSD(T)/aug-cc-pVDZ//MP2(FC)/aug-cc-pVDZ level. The $\Delta H_0^{\ddagger}$ for R9 calculated by M11-L/MG3S is 11.94 kcal/mol lower than that of OH + CF_3CHO at QCISD(T)/6-311G(d,p) level (Chandra et al., 2001). The present findings reveal that the much lower $\Delta H_0^{\ddagger}$ for R7-R9 leads to a much faster rate constant, indicating that oxidation by CH_2OO contributes significantly to the atmospheric loss of fluorinated aldehydes relative to the OH-initiated pathway from energetic point of view.

3.5. Kinetics

3.5.1 Pressure-dependent rate constants.

The pressure dependence of the rate constants for reactions R1 and R2 was evaluated using the ME/RRKM framework, with the results summarized in Tables S13–S15. As shown in Table S13, reaction R1 exhibits no appreciable pressure dependence over the conditions examined, indicating that pressure effects can be safely neglected for this channel. This conclusion is fully consistent with the findings reported by Luo et al (Luo et al., 2023). For example, the falloff factor calculated for the CH_2OO + HCHO reaction at 298 K and 0.0316 bar is 1.34 (Table S13). This factor, defined as the ratio of the rate constant at 1000 bar to that at 0.0316 bar, indicates only a weak pressure dependence for this system. This result is in excellent agreement with the findings reported by Luo et al. (Luo et al., 2023). We observed that at 295 K and 78 Torr, the pressure-

dependent rate constant was 2.71 × 10^{-11} cm^3 $molecule^{-1}$ s^{-1} in Table S13, which is 7.74 times higher than the reported value ((3.50 ± 0.35) × 10^{-12} cm^3 $molecule^{-1}$ s^{-1}) in Table 1 (Enders et al., 2024).

We assessed the validity of the simplified pathway by contrasting the full mechanism (Scheme 2a) with the model (Scheme 2b) from a kinetic perspective as listed in Tables S13 and S14. The pressure-dependent rate constants obtained from both models exhibit negligible deviations, thereby validating the simplified scheme as a computationally efficient strategy for larger aldehydes. The calculated pressure-dependent rate constant for reaction R2 is 1.84 × 10^{-12} cm^3 $molecule^{-1}$ s^{-1} at 293 K and 4 Torr in Table S14, in good agreement with the value of (9.50 ± 0.70) × 10^{-13} cm^3 $molecule^{-1}$ s^{-1} reported by Taatjes et al (Taatjes et al., 2012). Our pressure-dependent rate constant at 298 K and 25 Torr corroborates the experimental value of (1.20 ± 0.20) × 10^{-12} cm^3 $molecule^{-1}$ s^{-1} reported by Elsamra et al (1.65 × 10^{-12} cm^3 $molecule^{-1}$ s^{-1} in Table S14) (Elsamra et al., 2016). We found that the fall-off factor is only 1.36 (Table S14) for the reaction R2 at 298 K and 4 Torr, which also shown that the rate constant of reaction R2 is negligibly pressure-dependent, which confirms the experimental results qualitatively (Enders et al., 2024; Stone et al., 2014; Berndt et al., 2015; Jiang et al., 2024). In addition, there is experimental evidence that the pressure effect is also insignificant for propionaldehyde and butyraldehyde (Liu et al., 2020; Debnath and Rajakumar, 2024).

3.5.2 High pressure limit rate constants

High-pressure limit rate constants for all reactions are summarized in Table 5, with additional details provided in Tables S16–S24. The rate constants in the temperature range of 190–350 K were fitted using the four-parameter expression (Zheng and Truhlar, 2012; Bao et al., 2016a):

$$k_\infty = A\left(\frac{T+T_0}{300}\right)^n \exp\left[-\frac{E(T+T_0)}{R(T^2+{T_0}^2)}\right] \qquad (7)$$

Where R is the gas constant, T is temperature in K, the fitting parameters were listed in Table S25. The temperature dependence of the Arrhenius activation energies was further calculated using the following expression:

$$E_a = -R\frac{dlnk_\infty}{d(1/T)} \qquad (8)$$

Table 5. The high-pressure limiting rate constants (× 10^{-12} cm^3 $molecule^{-1}$ s^{-1}) of the CH_2OO + RCHO (R = H/CH_3/C_2H_5/C_3H_7/C_4H_9/C_5H_{12}/CH_2F/CHF_2/CF_3) reaction

T/K	k_1	k_2	k_3	k_4	k_5	k_6	k_7	k_8	k_9
200	426	96	105	115	106	214	430	451	740
220	297	32.7	36.1	40.8	36	71.9	248	416	688
240	171	13.6	15	17.5	14.8	29.5	115	381	652
260	90.4	65.4	7.27	8.72	6.75	13.1	51.1	328	626
280	48.0	3.55	3.93	4.86	3.64	7.09	24	252	607
298	28.3	2.27	2.45	3.10	2.28	4.46	13.1	182	594
300	26.8	2.11	2.34	2.97	2.22	4.41	12.3	174	593
320	15.9	1.35	1.49	1.95	1.37	2.67	6.90	110	583
340	10.0	9.22	1.01	1.35	0.93	1.80	4.17	67.4	576

The reaction of CH_2OO + HCHO. As summarized in Table 1 and Figure 1, a long-standing order-of-magnitude discrepancy exists between previously reported experimental and theoretical rate constants for reaction R1. At 296 K, the rate constant obtained in this work is 3.01×10^{-11} cm^3 molecule^{-1} s^{-1} in Table 1, which is 7.31 times larger than the experimental value reported by Luo et al (Luo et al., 2023), but 1.83 and 2.17 times smaller than the theoretical predictions of Zhang et al. (Zhang et al., 2023) and Long et al. (Long et al., 2021), respectively. We therefore consider two plausible explanations: The experimental determination of CH_2OO kinetics may introduce systematic uncertainties. Alternatively, subtle dynamic effects beyond conventional transition state theory (e.g., non-statistical dynamics or complex-forming behavior) may play a role and require further investigation. Although the present value does not fully reconcile the experimental and theoretical results, it substantially narrows the gap between the two, providing a quantitatively improved estimate for this key reaction.

Notably, the derived rate constant for R1 is approximately 8 times larger than that for the corresponding OH-initiated reaction and more than two orders of magnitude larger than that for the HO_2-initiated pathway (Long et al., 2022; Sivakumaran et al., 2003), highlighting the unexpectedly high reactivity of CH_2OO in this system. These findings underscore the need for further high-precision experimental measurements and establish the present computational protocol as a robust framework for resolving persistent discrepancies in atmospheric reaction kinetics.

The reaction of CH_2OO + CH_3CHO. To date, no theoretical kinetic studies have been reported for the CH_2OO + CH_3CHO reaction in Table 2. The earliest experimental determination yielded a rate constant of $(9.50 \pm 0.25) \times 10^{-13}$ cm^3 molecule^{-1} s^{-1} at 293 K and 4 Torr, as measured by Taatjes et al. (Taatjes et al., 2012), which is a factor of 2.9 smaller than the present theoretical prediction in Table 2. At 298 K, the calculated rate constant for reaction R2 is 2.50×10^{-12} cm^3 molecule^{-1} s^{-1} in

Table 2, in excellent agreement with the experimental values reported by Elsamra et al. (Elsamra et al., 2016) and Jiang et al. (Jiang et al., 2024) In addition, the value measured by Berndt et al. (Berndt et al., 2015) at 297 K, $(1.7 \pm 0.50) \times 10^{-12}$ cm^3 $molecule^{-1}$ s^{-1}, is fully consistent with our calculated result of 2.56×10^{-12} cm^3 $molecule^{-1}$ s^{-1} in Table 2. Overall, the rate constants obtained in this work are in good agreement with the available experimental data (Elsamra et al., 2016; Stone et al., 2014; Berndt et al., 2015; Jiang et al., 2024; Cornwell et al., 2023), providing the first reliable theoretical benchmark for the kinetics of the CH_2OO + CH_3CHO reaction. Notably, the rate constant for R2 is approximately 5.6 times smaller than that for the corresponding OH-initiated reaction, yet nearly two orders of magnitude larger than that for the HO_2-initiated pathway, highlighting the distinct and non-negligible role of CH_2OO in aldehyde oxidation chemistry (Long et al., 2022; Zhu et al., 2008). The five-membered ring species C2a and C2b readily interconvert, as the rate constant for the isomerization process is approximately two orders of magnitude larger than that of the addition reaction (Table S26).

The reaction of CH_2OO + RCHO (R=C_2H_5/C_3H_7/C_4H_9/C_5H_{11}). Rate constants for the reactions of CH_2OO with C_2H_5CHO have been reported previously from both experimental and theoretical studies (See Table 3) (Enders et al., 2024; Kaipara and Rajakumar, 2018; Liu et al., 2020), whereas the reaction with C_3H_7CHO has been examined only experimentally. At 298 K, the calculated rate constant for CH_2OO + C_2H_5CHO is 3.11×10^{-12} cm^3 $molecule^{-1}$ s^{-1} (Table 3), in excellent agreement with the experimental value reported by Liu et al (Liu et al., 2020).

For CH_2OO + C_3H_7CHO, the calculated rate constant of 3.10×10^{-12} cm^3 $molecule^{-1}$ s^{-1} (Table 3) closely reproduces the experimental value of $(2.63 \pm 0.14) \times 10^{-12}$ cm^3 $molecule^{-1}$ s^{-1} (Debnath and Rajakumar, 2024), further validating the reliability of the present computational protocol. To the best of our knowledge, no prior experimental or theoretical studies have reported rate constants for the reactions of CH_2OO with pentanal or hexanal. Our calculations indicate that the rate constant for CH_2OO + C_4H_9CHO is comparable to that for CH_3CHO, whereas the rate constant for CH_2OO + $C_5H_{11}CHO$ is approximately twice as large, yet remains within the same order of magnitude (Table 5). These results demonstrate that increasing alkyl chain length exerts only a minor influence on the reaction kinetics of CH_2OO with aldehydes, revealing a weak and nonmonotonic size dependence across the C_1–C_5 series. This behavior is fully consistent with the computed activation enthalpies (See Figure 2) and establishes a transferable structure–reactivity relationship for CH_2OO reactions with larger aldehydes. Overall, aside from formaldehyde, the rate constants for CH_2OO reactions with alkyl-substituted aldehydes vary only modestly, underscoring the

limited role of substituent size in governing CH_2OO reactivity.

The reaction of CH_2OO + RCHO (R=CH_2F/CHF_2/CHF_3). A striking fluorination-induced reactivity enhancement emerges upon substitution of hydrogen atoms on the methyl group. Introduction of fluorine leads to a pronounced increase in the rate constants for CH_2OO + CH_3CHO reactions, revealing an unexpected structure–reactivity trend. At 298 K, the rate constant for reaction R7 is 1.31×10^{-11} cm^3 $molecule^{-1}$ s^{-1} (Table 5), which is about 6 times larger than that of R2 and about 5 times larger than the corresponding OH + CH_2FCHO reaction (Lily et al., 2021).

Even more dramatic behavior is observed for reactions R8 and R9. For R8, the calculated rate constants approach the collision limit, decreasing slightly from 4.51×10^{-10} cm^3 $molecule^{-1}$ s^{-1} at 200 K to 6.75×10^{-11} cm^3 $molecule^{-1}$ s^{-1} at 340 K in Table 5, indicating of a weak negative temperature dependence characteristic of barrierless processes. Notably, at 298 K the reaction of CHF_2CHO with CH_2OO is more than two orders of magnitude faster than its reactions with OH [$(1.8 \pm 0.4) \times 10^{-12}$ cm^3 $molecule^{-1}$ s^{-1}] (Sellevåg et al., 2005), underscoring the unusually high reactivity of CH_2OO toward fluorinated aldehydes.

The most pronounced effect is found for R9, for which the rate constant ranges from 7.40×10^{-10} cm^3 $molecule^{-1}$ s^{-1} at 200 K to 5.76×10^{-10} cm^3 $molecule^{-1}$ s^{-1} at 340 K in Table 5, fully approaching the collision limit and exceeding the corresponding OH-initiated reaction rates by orders of magnitude. These results demonstrate that fluorination fundamentally alters the reaction landscape of CH_2OO with aldehydes, transforming otherwise moderately fast bimolecular reactions into near-collision-controlled processes.

3.6. Atmospheric Implications

The reaction of aldehydes with OH have been investigated extensively experimentally and theoretically. Here, we considered the competition for aldehydes relative to CH_2OO and OH. the ratio of reaction rate was calculated by eqn (9):

$$v_{\mathrm{i}} = \frac{k_i[\mathrm{CH_2OO}]}{k_{\mathrm{OH},i}[\mathrm{OH}]} \qquad (9)$$

where the k_i is the rate constants for the reaction R2-R9, $k_{OH,i}$ is the rate constant of OH + RCHO (R = CH_3, C_2H_5, C_3H_7, C_4H_9, C_5H_{11}, CH_2F, CHF_2, CF_3), and i is referred to is equal to 2-9. The concentrations of CH_2OO and OH exhibit pronounced geographical and spatial distributions. The concentration of OH is varied from 10^4-10^6 molecules cm^{-3} (Khan et al., 2018; Ren et al., 2003; Stone et al., 2012), and the estimated concentration for CH_2OO is range from 10^4 to 10^5 molecules cm^{-3} (peaking

at 6×10^5 molecules cm^{-3}) (Lelieveld et al., 2016; Novelli et al., 2017) In contrast, the base-version model simulations yield CH_2OO concentrations approximately one order of magnitude lower than the estimated value. This discrepancy likely originates from (i) the adoption of relatively fast rate constants for CH_2OO loss via reactions with H_2O and $(H_2O)_2$, and (ii) an incomplete representation of CH_2OO sources in the model framework. Consequently, the use of model-derived concentrations probably leads to an underestimation of the contribution of CH_2OO to aldehyde removal.

Our results demonstrate that for aliphatic aldehydes, reactions with CH_2OO constitute a negligible sink compared with OH oxidation, owing to both modest rate constants and low ambient CH_2OO concentration (See Tables S27–S29). Although fluorine substitution generally enhances reactivity, the increase in the rate constant for CH_2FCHO remains insufficient to meaningfully compete with the OH pathway. Effective competition is predicted only under highly specific conditions—namely, nighttime at ~10 km altitude over the Malaysian region (Table 6). In stark contrast, the reactions of highly fluorinated aldehydes with CH_2OO proceed at near-collision-limit rates. As a result, CH_2OO constitutes a major atmospheric sink for CHF_2CHO and CF_3CHO. As summarized in Table 6, CH_2OO competes effectively with OH for CHF_2CHO at night near the surface over Russia and the Arctic, influences its removal at 5 km over Russia and Indonesia, and contributes significantly at 10 km over Indonesia. Notably, because the reaction of CF_3CHO with OH is intrinsically slow, CH_2OO dominates its atmospheric removal over Indonesia at all altitudes considered, while in the Russian region its influence is confined to 0 and 5 km.

Table 6. rate concentration ratios CH_2OO to OH and the rate ratio at different heights from different region

Height	T/K	P/mBar	$[CH_2OO]/[OH]^a$	$v_8{}^b$	$v_9{}^c$
Gansu, China					
1	290.2	1013	2.48×10^{-4}	2.89×10^{-2}	2.29×10^{-1}
5	250.5	495.9	3.09×10^{-4}	6.25×10^{-2}	3.03×10^{-1}
10	215.6	242.8	3.51×10^{-5}	8.14×10^{-3}	3.77×10^{-2}
Russia					
1	290.2	1013	1.52×10^{-2}	1.77	14
5	250.5	495.9	6.39×10^{-3}	1.29	6.26
10	215.6	242.8	3.23×10^{-5}	7.48×10^{-3}	3.47×10^{-2}
Arctic					
1	290.2	1013	1.15×10^{-2}	1.33	10.6
5	250.5	495.9	5.16×10^{-4}	1.04×10^{-1}	5.05×10^{-1}
10	215.6	242.8	1.91×10^{-6}	4.43×10^{-4}	2.05×10^{-3}

Indonesia					
1	290.2	1013	3.16×10^{-3}	3.67×10^{-1}	2.91
5	250.5	495.9	5.85×10^{-3}	1.18	5.74
10	215.6	242.8	2.53×10^{-2}	5.87	27.2

[a]The concentration ratio between CH_2OO and OH from GEOS-Chem.

[b]The rate ratio between CH_2OO + CHF_2CHO and CHF_2CHO + OH.

[c]The rate ration between CH_2OO + CF_3CHO and CF_3CHO + OH.

Overall, these findings reveal a qualitative shift in aldehyde oxidation pathways upon heavy fluorination, identifying CH_2OO as a previously underappreciated but potentially dominant oxidant for highly fluorinated aldehydes under specific atmospheric regimes—an effect with important implications for the atmospheric lifetimes of emerging fluorinated oxygenated VOCs.

3.7. Atmospheric modelling

Model simulations were further performed to assess the atmospheric significance of nighttime reactions between CH_2OO and aldehydes. The Criegee intermediate (CI) chemistry implemented in the base model has been described in our previous work (Long et al., 2024). In this study, two targeted updates were introduced to isolate and quantify the impacts of newly identified CI–aldehyde reaction pathways. The first update incorporates the CH_2OO + HCHO reaction into the base mechanism, reflecting an improved understanding of CI removal under aldehyde-rich nighttime conditions. The second update further expands the CI sink by including the reaction between CH_2OO and CH_3CHO, thereby providing a more comprehensive representation of acetaldehyde-driven CI loss. The aldehyde chemistry employed in the model is summarized in Table S30. We do not consider the impact of CH_2OO on fluorinated aldehyde sinks by using GEOS-Chem, as fluorinated aldehydes are not involved in the current default GEOS-Chem version.

The simulated aldehyde concentrations exhibit pronounced spatial and vertical heterogeneity. Surface-level HCHO concentrations reach up to 1.46×10^{11} molecules cm^{-3}, while CH_3CHO attains maxima of 8.06×10^{10} molecules cm^{-3}, with the highest abundances over Malaysia and Indonesia. These values are consistent with field observations, which report peak HCHO concentrations of up to 3.63×10^{11} molecules cm^{-3} (Hu et al., 2025), lending confidence to the model performance. The simulated global mean surface concentration of CH_3CHO (5.89×10^9 molecules cm^{-3}, corresponding to ~200 ppt) is in

reasonable agreement with observational constraints and remains lower than values reported by Komazaki et al (Komazaki et al., 1999; Tereszchuk and Bernath, 2011).

The contribution of HCHO to the reduction of CH_2OO has been assessed in our prior work and is once again validated by model simulations (Long et al., 2021). Figure 5 shows the relative changes in annual mean surface-layer CH_2OO concentrations resulting from the inclusion of the CH_2OO + HCHO (R1) and CH_2OO + CH_3CHO (R2) reactions. Incorporation of the updated rate constant for R1 leads to a pronounced reduction in CH_2OO, with a maximum decrease of 25.3% over the Antarctic region (Figure 5), highlighting the previously unrecognized importance of HCHO as a nighttime CI sink. In contrast, R2 produces a more modest effect, with a maximum CH_2OO reduction of 3.39% over Russia in Figure 5.

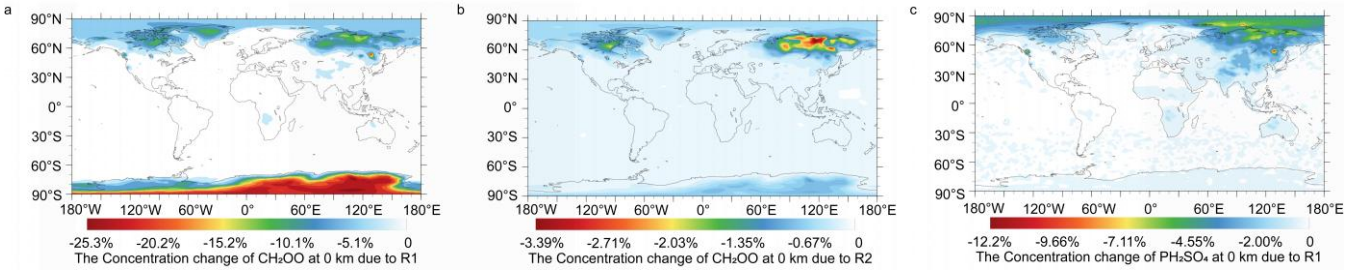

Figure 5. Changes in global CH_2OO concentrations due to reaction R1 and R2 (a) reaction R1, (b) reaction R2, and (c) changes in global sulfate concentrations due to reaction R1.

Despite the substantial impact on CI abundances, the direct effects on aldehyde concentrations remain small. As shown in Figure S8, surface acetaldehyde decreases by only 0.12% in the Arctic. However, the influence on secondary oxygenated products is more pronounced. As illustrated in Figure S9, inclusion of R1 enhances formic acid concentrations by up to 5.44% over Canada and Russia, while acetic acid increases by as much as 0.69% in the Arctic. These results demonstrate that CI–aldehyde reactions, while exerting limited feedback on aldehydes themselves, can make significant contribution to the sinks of CH_2OO and the formation of atmospheric acids.

The potential implications of reaction R1 for regional air quality were also assessed, particularly regarding the mitigation of gas-phase sulfate formation. We found that the concentration of gas-phase sulfate can reach 10^8 molecules cm^{-3} in Mexico region in Figure S10. The inclusion of this reaction pathway effectively lowers the concentration of CH_2OO, thereby diminishing its capacity to oxidize SO_2 into sulfuric acid precursors. This depletion of oxidative capacity leads to a marked decrease in gas-phase sulfate concentration. The effect is geographical, with the reduction in gas-phase sulfate concentrations

estimated to be 12.2% in Canada and 6.01% in Russia during the nighttime in Figure 5c. While the relative changes might initially imply a substantial regional sink for atmospheric sulfate aerosols, a detailed comparison of Figures 5c and S10 reveals that the largest percentage changes in gas-phase sulfate predominantly occur in regions with low baseline concentrations. Specifically, although peak concentrations over Canada and Russia reach ~10^7 molecules cm^{-3}, their regional averages remain on the order of 10^5 molecules cm^{-3}. In contrast, regions with much higher absolute concentrations (e.g., ~1×10^8 molecules cm^{-3} over Mexico) exhibit only minimal relative changes. This indicates that modest absolute variations can produce large percentage changes under low-background conditions, whereas comparable or even larger absolute changes appear insignificant in high-concentration environments. Consequently, this reaction has a negligible impact on the global atmospheric sulfate burden.

4. CONCLUSIONS

The present work establishes a transferable and systematically improvable theoretical framework for predicting quantitative atmospheric reaction kinetics across molecular complexity, using the reactions of CH_2OO with a series of aldehydes as a definitive test case. By explicitly approaching the full configuration interaction (CI) limit for the benchmark CH_2OO + HCHO system, we delineate the accuracy requirements necessary for reliable kinetic predictions and provide a rigorous reference against which lower-cost methods can be assessed. Energetic and kinetic analyses validate a simplified reaction mechanism, attributed to the facile interconversion between complexes and the energetic preference for rotational transition states over addition pathways.

Guided by the detailed electronic-structure insights obtained for CH_2OO + HCHO, we develop a computational protocol that integrates optimized geometries, vibrational frequencies, and high-level single-point energies, enabling accurate kinetics for larger systems at feasible computational cost. We find that DF-CCSD(T)-F12b/VDZ(d) and DF-CCSD(T)-F12b/jun-cc-pVDZ can be used to reliably describe the optimized geometries and calculated frequencies. two generalizable strategies (BE1 and BE2) have been used to recover the CCSDTQ/CBS level single point energies, which provide new insight into how to obtain the quantitative enthalpy of activation.

In kinetics calculations, for reactions with appreciable barriers (R2–R6), this dual-level strategy yields robust rate constants, whereas for reactions characterized by exceptionally low or submerged barriers (R1 and R7–R9), the explicit application of VRC-VTST proves essential for capturing the correct dynamical behavior. This demonstrates a practical pathway for extending benchmark-level kinetics from small to chemically diverse, larger molecules.

The resulting kinetic trends reveal that alkyl-chain elongation exerts only a minor influence on reactivity, whereas fluorine substitution dramatically enhances reaction rates, driving the CH_2OO + CHF_2CHO and CH_2OO + CF_3CHO reactions toward the collision limit. All reactions exhibit negligible pressure dependence, underscoring their relevance under atmospheric conditions. These high-precision rate constants provide a mechanistically grounded explanation for the increasingly important role of Criegee intermediates in the oxidation of fluorinated aldehydes. We find that fluorine substitution on aldehydes dramatically enhances their reactivity toward CH_2OO; however, the post-CCSD(T) contributions remain almost equal across the reaction series. This behavior indicates that fluorination-driven rate acceleration is governed primarily by lower-level electronic effects rather than by higher-order electron correlation than CCSD(T). This observation also provides a fundamental basis for the development of high-accuracy semiempirical correction schemes.

Beyond molecular-scale kinetics, global and regional modeling demonstrates that while reactions of CH_2OO with HCHO and CH_3CHO contribute negligibly to aldehyde removal, HCHO constitutes a major global sink for Criegee intermediates, accounting for a 25.3% reduction in the global CH_2OO burden during the night. In contrast, fluorination fundamentally alters atmospheric fate: for CH_2FCHO, CH_2OO reactions become regionally significant (e.g., near 10 km altitude over Malaysia), and for more heavily fluorinated aldehydes such as CHF_2CHO, CH_2OO overwhelmingly dominates over OH-initiated loss pathways. The associated enhancement in acid formation, although modest, further highlights the chemical implications of these processes. The inclusion of reaction R1 results in a reduction of gas-phase sulfate levels by 12.2% over Canada and 6.01% over Russia. These present findings deliver a generalizable, benchmark-anchored strategy for quantitative kinetic prediction, bridges electronic-structure theory with atmospheric modeling, and reveals how fluorination reshapes the atmospheric relevance of Criegee intermediates—insights that are critical for atmospheric chemical mechanisms.

Supplement. The following information is provided in the Supplement: Details of reaction R9, enthalpies of binding and activation and barrier height; vibrational frequency scale factors; Lennard-Jone parameters; Rate constants and rate constant fits; Rate ratio; Absolute energies and the Cartesian coordinates and absolute energies; relative enthalpies for reaction of R3-R9; Enthalpy profile for the conversion of pre-reaction complex; Changes in global CH_3CHO, HCOOH, and CH_3COOH concentrations.

Data and code availability. Electronic structure calculations were performed using commercially available software (Gaussian 16, Revision A.03 and Molpro 2019). Access to the software is subject to licensing terms. The MRCC and MSTor codes can be accessed at https://www.mrcc.hu and https://comp.chem.umn.edu/mstor, respectively. Polyrate 2017-C and Gaussrate 2017-B are available at https://comp.chem.umn.edu/polyrate and https://comp.chem.umn.edu/gaussrate. KiSThlP 2021 is accessible at http://kisthelp.univ-reims.fr, and the TUMME program can be found at https://comp.chem.umn.edu/tumme. The GEOS-Chem 14.4.2 is available at http://www.geos-chem.org. Optimized geometries, and calculated energies are available in Supplement. Other data are available from the corresponding author upon reasonable request.

Author contributions. CX carried out the calculations, analysed and interpretation of data, and wrote the manuscript draft. BL designed the project, analysed and inerpretation of data, and reviewed and edited the manuscript.

Competing interests. The authors declare that they have no conflict of interest.

Acknowledgements. We also thank the Minnesota Supercomputing Institute for computational resources

Financial support. This work was supported in part by the National Natural Science Foundation of China (42120104007 and 41775125), by the Guizhou Provincial Science and Technology Projects, China (CXTD [2022]001 and GCC [2023]026), and by the U.S. Department of Energy under Award DE-SC0015997, Guizhou Graduate Research Fund Project under Grant 2024YJSK YJJ224.

Reference

Adler, T. B., Knizia, G., and Werner, H.-J.: A simple and efficient CCSD(T)-F12 approximation, J. Chem. Phys., 127, 221106, https://doi.org/10.1063/1.2817618, 2007.

Atkinson, R. and Pitts, J. N., Jr.: Kinetics of the reactions of the OH radical with HCHO and CH_3CHO over the temperature range 299–426 K, J. Chem. Phys., 68, 3581-3584, https://doi.org/10.1063/1.436215, 1978.

Bao, J., Zhang, X., Wu, Z., Zhou, L., Qian, J., Tan, Q., Yang, F., Chen, J., Li, Y., Liu, H., Deng, L., and Li, H.: Atmospheric carbonyl compounds are crucial in regional ozone heavy pollution: insights from the Chengdu Plain Urban Agglomeration, China, Atmos. Chem. Phys., 25, 1899-1916, https://doi.org/10.5194/acp-25-1899-2025, 2025.

Bao, J. L., Zhang, X., and Truhlar, D. G.: Predicting pressure-dependent unimolecular rate constants using variational transition state theory with multidimensional tunneling combined with system-specific quantum RRK theory: a definitive test for fluoroform dissociation, Phys. Chem. Chem. Phys., 18, 16659-16670, https://doi.org/10.1039/C6CP02765B, 2016a.

Bao, J. L., Zhang, X., and Truhlar, D. G.: Barrierless association of CF_2 and dissociation of C_2F_4 by variational transition-state theory and system-specific quantum Rice–Ramsperger–Kassel theory, Proc. Natl. Acad. Sci., 113, 13606-13611, https://doi.org/10.1073/pnas.1616208113, 2016b.

Bari, M. A. and Kindzierski, W. B.: Ambient volatile organic compounds (VOCs) in Calgary, Alberta: Sources and screening health risk assessment, Sci. Total Environ., 631-632, 627-640, https://doi.org/10.1016/j.scitotenv.2018.03.023, 2018.

Berndt, T., Jokinen, T., Sipilä, M., Mauldin, R. L., Herrmann, H., Stratmann, F., Junninen, H., and Kulmala, M.: H_2SO_4 formation from the gas-phase reaction of stabilized Criegee Intermediates with SO_2: Influence of water vapour content and temperature, Atmos. Environ., 89, 603-612, https://doi.org/10.1016/j.atmosenv.2014.02.062, 2014.

Berndt, T., Kaethner, R., Voigtländer, J., Stratmann, F., Pfeifle, M., Reichle, P., Sipilä, M., Kulmala, M., and Olzmann, M.: Kinetics of the unimolecular reaction of CH_2OO and the bimolecular reactions with the water monomer, acetaldehyde and acetone under atmospheric conditions, Phys. Chem. Chem. Phys., 17, 19862-19873, https://doi.org/10.1039/C5CP02224J, 2015.

Bey, I., Jacob, D. J., Yantosca, R. M., Logan, J. A., Field, B. D., Fiore, A. M., Li, Q., Liu, H. Y., Mickley, L. J., and Schultz, M. G.: Global modeling of tropospheric chemistry with assimilated meteorology: Model description and evaluation, J. Geophys. Res.: Atmos., 106, 23073-23095, https://doi.org/10.1029/2001JD000807, 2001.

Bischoff, F. A., Wolfsegger, S., Tew, D. P., and Klopper, W.: Assessment of basis sets for F12 explicitly-correlated molecular electronic-structure methods, Mol. Phys., 107, 963-975, https://doi.org/10.1080/00268970802708942, 2009.

Bossmeyer, J., Brauers, T., Richter, C., Rohrer, F., Wegener, R., and Wahner, A.: Simulation chamber studies on the NO_3 chemistry of atmospheric aldehydes, Geophys. Res. Lett., 33, https://doi.org/10.1029/2006GL026778, 2006.

Boy, M., Mogensen, D., Smolander, S., Zhou, L., Nieminen, T., Paasonen, P., Plass-Dülmer, C., Sipilä, M., Petäjä, T., Mauldin, L., Berresheim, H., and Kulmala, M.: Oxidation of SO_2 by stabilized Criegee intermediate (sCI) radicals as a crucial source for atmospheric sulfuric acid concentrations, Atmos. Chem. Phys., 13, 3865-3879, https://doi.org/10.5194/acp-13-3865-2013, 2013.

Cabañas, B., Martín, P., Salgado, S., Ballesteros, B., and Martínez, E.: An Experimental Study on the Temperature Dependence for the Gas-Phase Reactions of NO_3 Radical with a Series of Aliphatic Aldehydes, J. Atmos. Chem., 40, 23-39, https://doi.org/10.1023/A:1010797424283, 2001.

Cabezas, C. and Endo, Y.: The Criegee intermediate-formic acid reaction explored by rotational spectroscopy, Phys. Chem. Chem. Phys., 21, 18059-18064, https://doi.org/10.1039/C9CP03001H, 2019.

Canneaux, S., Bohr, F., and Henon, E.: KiSThelP: A program to predict thermodynamic properties and rate constants from quantum chemistry results, J. Comput. Chem., 35, 82-93, https://doi.org/10.1002/jcc.23470, 2014.

Chan, B. and Radom, L.: W2X and W3X-L: Cost-Effective Approximations to W2 and W4 with kJ mol^{-1} Accuracy, J. Chem. Theory Comput., 11, 2109-2119, https://doi.org/10.1021/acs.jctc.5b00135, 2015.

Chandra, A. K., Uchimaru, T., and Sugie, M.: Kinetics of hydrogen abstraction reactions of CF_3CHO, CF_2ClCHO, $CFCl_2CHO$ and CCl_3CHO with OH Radicals: An ab initio study, Phys. Chem. Chem. Phys., 3, 3961-3966, https://doi.org/10.1039/B104904F, 2001.

Chen, W. T., Shao, M., Lu, S. H., Wang, M., Zeng, L. M., Yuan, B., and Liu, Y.: Understanding primary and secondary sources of ambient carbonyl compounds in Beijing using the PMF model, Atmos. Chem. Phys., 14, 3047-3062, https://doi.org/10.5194/acp-14-3047-2014, 2014.

Chhantyal-Pun, R., Khan, M. A. H., Zachhuber, N., Percival, C. J., Shallcross, D. E., and Orr-Ewing, A. J.: Impact of Criegee Intermediate Reactions with Peroxy Radicals on Tropospheric Organic Aerosol, ACS Earth Space Chem., 4, 1743-1755, https://doi.org/10.1021/acsearthspacechem.0c00147, 2020.

Chung, C.-A., Su, J. W., and Lee, Y.-P.: Detailed mechanism and kinetics of the reaction of Criegee intermediate CH_2OO with HCOOH investigated via infrared identification of conformers of hydroperoxymethyl formate and formic acid anhydride, Phys. Chem. Chem. Phys., 21, 21445-21455, https://doi.org/10.1039/C9CP04168K, 2019.

Cornwell, Z. A., Enders, J. J., Harrison, A. W., and Murray, C.: Temperature-dependent kinetics of the reactions of CH_2OO with acetone, biacetyl, and acetylacetone, Int. J. Chem. Kinet., 55, 154-166, https://doi.org/10.1002/kin.21625, 2023.

Criegee, R.: Mechanism of Ozonolysis, Angew. Chem. Int. Ed., 14, 745-752, https://doi.org/10.1002/anie.197507451, 1975.

Criegee, R. and Wenner, G.: Die Ozonisierung des 9,10-Oktalins, Justus Liebigs Ann. Chem., 564, 9-15, https://doi.org/10.1002/jlac.19495640103, 1949.

D'Anna, B., Andresen, Ø., Gefen, Z., and Nielsen, C. J.: Kinetic study of OH and NO_3 radical reactions with 14 aliphatic aldehydes, Phys. Chem. Chem. Phys., 3, 3057-3063, https://doi.org/10.1039/B103623H, 2001.

Debnath, A. and Rajakumar, B.: Experimental and theoretical study of Criegee intermediate (CH_2OO) reactions with n-butyraldehyde and isobutyraldehyde: kinetics, implications and atmospheric fate, Phys. Chem. Chem. Phys., 26, 6872-6884, https://doi.org/10.1039/D3CP05482A, 2024.

Ding, D.-P. and Long, B.: Reaction between propionaldehyde and hydroxyperoxy radical in the atmosphere: A reaction route for the sink of propionaldehyde and the formation of formic acid, Atmos. Environ., 284, 119202, https://doi.org/10.1016/j.atmosenv.2022.119202, 2022.

Edwards, P. M., Brown, S. S., Roberts, J. M., Ahmadov, R., Banta, R. M., deGouw, J. A., Dubé, W. P., Field, R. A., Flynn, J. H., Gilman, J. B., Graus, M., Helmig, D., Koss, A., Langford, A. O., Lefer, B. L., Lerner, B. M., Li, R., Li, S.-M., McKeen, S. A., Murphy, S. M., Parrish, D. D., Senff, C. J., Soltis, J., Stutz, J., Sweeney, C., Thompson, C. R., Trainer, M. K., Tsai, C.,

Veres, P. R., Washenfelder, R. A., Warneke, C., Wild, R. J., Young, C. J., Yuan, B., and Zamora, R.: High winter ozone pollution from carbonyl photolysis in an oil and gas basin, Nature, 514, 351-354, https://doi.org/10.1038/nature13767, 2014.

Elsamra, R. M. I., Jalan, A., Buras, Z. J., Middaugh, J. E., and Green, W. H.: Temperature- and Pressure-Dependent Kinetics of CH_2OO + CH_3COCH_3 and CH_2OO + CH_3CHO: Direct Measurements and Theoretical Analysis, Int. J. Chem. Kinet., 48, 474-488, https://doi.org/10.1002/kin.21007, 2016.

Enders, J. J., Cornwell, Z. A., Harrison, A. W., and Murray, C.: Temperature-Dependent Kinetics of the Reactions of the Criegee Intermediate CH_2OO with Aliphatic Aldehydes, J. Phys. Chem. A, 128, 7879-7888, https://doi.org/10.1021/acs.jpca.4c04990, 2024.

Fernández-Ramos, A., Miller, J. A., Klippenstein, S. J., and Truhlar, D. G.: Modeling the Kinetics of Bimolecular Reactions, Chem. Rev., 106, 4518-4584, https://doi.org/10.1021/cr050205w, 2006.

Foreman, E. S., Kapnas, K. M., and Murray, C.: Reactions between Criegee Intermediates and the Inorganic Acids HCl and HNO3: Kinetics and Atmospheric Implications, Angew. Chem. Int. Ed., 55, 10419-10422, https://doi.org/10.1002/anie.201604662, 2016.

Frisch, M. J., Trucks, G. W., Schlegel, H. B., Scuseria, G. E., Robb, M. A., Cheeseman, J. R., Scalmani, G., Barone, V., Mennucci, B., Petersson, G. A., Nakatsuji, H., Caricato, M., Li, X., Hratchian, H. P., Izmaylov, A. F., Bloino, J., Zheng, G., Sonnenberg, J. L., Hada, M., Ehara, M., Toyota, K., Fukuda, ., Hasegawa, J., Ishida, M., Nakajima, T., Honda, Y., Kitao, O., Nakai, H., Vreven, T., Montgomery, J. A., Peralta, J. E., Ogliaro, F., Bearpark, M., Heyd, J. J., Brothers, E., Kudin, K. N., Staroverov, V. N., Kobayashi, R., Normand, J., Raghavachari, K., Rendell, A., Burant, J. C., Iyengar, S. S., Tomasi, J., Cossi, M., Rega, N., Millam, J. M., Klene, M., Knox, J. E., Cross, J. B., Bakken, V., Adamo, C., Jaramillo, J., Gomperts, R., Stratmann, R. E., Yazyev, O., Austin, A. J., Cammi, R., Pomelli, C., Ochterski, J. W., Martin, R. L., Morokuma, K., Zakrzewski, V. G., Voth, G. A., Salvador, P., Dannenberg, J. J., Dapprich, S., Daniels, A. D., Farkas, O., Foresman, J. B., Ortiz, J. V., Cioslowski, J., and Fox, D. J.: Gaussian 16, Revision A.03, Gaussian Inc, Wallingford CT, https://gaussian.com/gaussian16/ (last access: 20 November 2023), 2016.

Gao, Q., Shen, C., Zhang, H., Long, B., and Truhlar, D. G.: Quantitative kinetics reveal that reactions of HO_2 are a significant sink for aldehydes in the atmosphere and may initiate the formation of highly oxygenated molecules via autoxidation, Phys. Chem. Chem. Phys., 26, 16160-16174, https://doi.org/10.1039/D4CP00693C, 2024.

Garrett, B. C. and Truhlar, D. G.: Canonical unified statistical model. Classical mechanical theory and applications to collinear reactions, J. Chem. Phys., 76, 1853-1858, https://doi.org/10.1063/1.443157, 1982.

Gelaro, R., McCarty, W., Suárez, M. J., Todling, R., Molod, A., Takacs, L., Randles, C. A., Darmenov, A., Bosilovich, M. G., Reichle, R., Wargan, K., Coy, L., Cullather, R., Draper, C., Akella, S., Buchard, V., Conaty, A., da Silva, A. M., Gu, W., Kim, G.-K., Koster, R., Lucchesi, R., Merkova, D., Nielsen, J. E., Partyka, G., Pawson, S., Putman, W., Rienecker, M., Schubert, S. D., Sienkiewicz, M., and Zhao, B.: The Modern-Era Retrospective Analysis for Research and Applications, Version 2 (MERRA-2), J. Clim., 30, 5419-5454, https://doi.org/10.1175/JCLI-D-16-0758.1, 2017.

Georgievskii, Y. and Klippenstein, S. J.: Variable reaction coordinate transition state theory: Analytic results and application to the C_2H_3+H→C_2H_4 reaction, J. Chem. Phys., 118, 5442-5455, https://doi.org/10.1063/1.1539035, 2003.

Georgievskii, Y., Miller, J. A., Burke, M. P., and Klippenstein, S. J.: Reformulation and Solution of the Master Equation for Multiple-Well Chemical Reactions, J. Phys. Chem. A, 117, 12146-12154, https://doi.org/10.1021/jp4060704, 2013.

Grosjean, D., Swanson, R. D., and Ellis, C.: Carbonyls in Los Angeles air: Contribution of direct emissions and photochemistry, Sci. Total Environ., 29, 65-85, https://doi.org/10.1016/0048-9697(83)90034-7, 1983.

Guenther, A. B., Jiang, X., Heald, C. L., Sakulyanontvittaya, T., Duhl, T., Emmons, L. K., and Wang, X.: The Model of Emissions of Gases and Aerosols from Nature version 2.1 (MEGAN2.1): an extended and updated framework for modeling biogenic emissions, Geosci. Model Dev., 5, 1471-1492, https://doi.org/10.5194/gmd-5-1471-2012, 2012.

Győrffy, W. and Werner, H.-J.: Analytical energy gradients for explicitly correlated wave functions. II. Explicitly correlated coupled cluster singles and doubles with perturbative triples corrections: CCSD(T)-F12, J. Chem. Phys., 148, 114104, https://doi.org/10.1063/1.5020436, 2018.

Hoesly, R. M., Smith, S. J., Feng, L., Klimont, Z., Janssens-Maenhout, G., Pitkanen, T., Seibert, J. J., Vu, L., Andres, R. J., Bolt, R. M., Bond, T. C., Dawidowski, L., Kholod, N., Kurokawa, J. I., Li, M., Liu, L., Lu, Z., Moura, M. C. P., O'Rourke, P. R., and Zhang, Q.: Historical (1750–2014) anthropogenic emissions of reactive gases and aerosols from the Community Emissions Data System (CEDS), Geosci. Model Dev., 11, 369-408, https://doi.org/10.5194/gmd-11-369-2018, 2018.

Hu, R., Zhang, G., Cai, H., Guo, J., Lu, K., Li, X., Lou, S., Tan, Z., Hu, C., Xie, P., and Liu, W.: Accurate elucidation of oxidation under heavy ozone pollution: a full suite of radical measurements in the chemically complex atmosphere, Atmos. Chem. Phys., 25, 3011-3028, https://doi.org/10.5194/acp-25-3011-2025, 2025.

Jalan, A., Allen, J. W., and Green, W. H.: Chemically activated formation of organic acids in reactions of the Criegee intermediate with aldehydes and ketones, Phys. Chem. Chem. Phys., 15, 16841-16852, https://doi.org/10.1039/C3CP52598H, 2013.

Jenkin, M. E., Valorso, R., Aumont, B., Rickard, A. R., and Wallington, T. J.: Estimation of rate coefficients and branching ratios for gas-phase reactions of OH with aromatic organic compounds for use in automated mechanism construction, Atmos. Chem. Phys., 18, 9329-9349, https://doi.org/10.5194/acp-18-9329-2018, 2018.

Jiang, H., Liu, Y., Xiao, C., Yang, X., and Dong, W.: Reaction Kinetics of CH_2OO and syn-CH_3CHOO Criegee Intermediates with Acetaldehyde, J. Phys. Chem. A, 128, 4956-4965, https://doi.org/10.1021/acs.jpca.4c01374, 2024.

Jiménez, E., Lanza, B., Martínez, E., and Albaladejo, J.: Daytime tropospheric loss of hexanal and trans-2-hexenal: OH kinetics and UV photolysis, Atmos. Chem. Phys., 7, 1565-1574, https://doi.org/10.5194/acp-7-1565-2007, 2007.

Kaipara, R. and Rajakumar, B.: Temperature-Dependent Kinetics of the Reaction of a Criegee Intermediate with Propionaldehyde: A Computational Investigation, J. Phys. Chem. A, 122, 8433-8445, https://doi.org/10.1021/acs.jpca.8b06603, 2018.

Kállay, M., Nagy, P. R., Mester, D., Rolik, Z., Samu, G., Csontos, J., Csóka, J., Szabó, P. B., Gyevi-Nagy, L., Hégely, B., Ladjánszki, I., Szegedy, L., Ladóczki, B., Petrov, K., Farkas, M., Mezei, P. D., and Ganyecz, Á.: The MRCC program system: Accurate quantum chemistry from water to proteins, J. Chem. Phys., 152, 074107, https://doi.org/10.1063/1.5142048, 2020.

Kenneth A. Holbrook, M. J. P., Struan H. Robertson Unimolecular Reactions, 2nd ed., John Wiley & Sons: Chichester, pp, 177− 214, 1996.

Khan, M. A. H., Percival, C. J., Caravan, R. L., Taatjes, C. A., and Shallcross, D. E.: Criegee intermediates and their impacts on the troposphere, Environ. Sci. Processes Impacts, 20, 437-453, https://doi.org/10.1039/C7EM00585G, 2018.

Klippenstein, S. J.: RRKM theory and its implementation, in: Comprehensive Chemical Kinetics, Elsevier, pp, 55-103, 2003.

Knizia, G., Adler, T. B., and Werner, H.-J.: Simplified CCSD(T)-F12 methods: Theory and benchmarks, J. Chem. Phys., 130,

698 054104, 10.1063/1.3054300, 2009.
699 Knote, C., Hodzic, A., Jimenez, J. L., Volkamer, R., Orlando, J. J., Baidar, S., Brioude, J., Fast, J., Gentner, D. R., Goldstein,
700 A. H., Hayes, P. L., Knighton, W. B., Oetjen, H., Setyan, A., Stark, H., Thalman, R., Tyndall, G., Washenfelder, R., Waxman,
701 E., and Zhang, Q.: Simulation of semi-explicit mechanisms of SOA formation from glyoxal in aerosol in a 3-D model, Atmos.
702 Chem. Phys., 14, 6213-6239, https://doi.org/10.5194/acp-14-6213-2014, 2014.
703 Komazaki, Y., Hiratsuka, M., Narita, Y., Tanaka, S., and Fujita, T.: The development of an automated continuous measurement
704 system for the monitoring of HCHO and CH_3CHO in the atmosphere by using an annular diffusion scrubber coupled to HPLC,
705 Fresenius' J. Anal. Chem., 363, 686-695, https://doi.org/10.1007/s002160051272, 1999.
706 Kukui, A., Chartier, M., Wang, J., Chen, H., Dusanter, S., Sauvage, S., Michoud, V., Locoge, N., Gros, V., Bourrianne, T.,
707 Sellegri, K., and Pichon, J. M.: Role of Criegee intermediates in the formation of sulfuric acid at a Mediterranean (Cape Corsica)
708 site under influence of biogenic emissions, Atmos. Chem. Phys., 21, 13333-13351, https://doi.org/10.5194/acp-21-13333-2021,
709 2021.
710 Lary, D. J. and Shallcross, D. E.: Central role of carbonyl compounds in atmospheric chemistry, J. Geophys. Res.: Atmos., 105,
711 19771-19778, https://doi.org/10.1029/1999JD901184, 2000.
712 Lelieveld, J., Gromov, S., Pozzer, A., and Taraborrelli, D.: Global tropospheric hydroxyl distribution, budget and reactivity,
713 Atmos. Chem. Phys., 16, 12477-12493, https://doi.org/10.5194/acp-16-12477-2016, 2016.
714 Li, F., Tang, S., Lv, J., Yu, S., Sun, X., Cao, D., Wang, Y., and Jiang, G.: Critical contribution of chemically diverse carbonyl
715 molecules to the oxidative potential of atmospheric aerosols, Atmos. Chem. Phys., 24, 8397-8411, https://doi.org/10.5194/acp-
716 24-8397-2024, 2024.
717 Lily, M., Hynniewta, S., Muthiah, B., Wang, W., Chandra, A. K., and Liu, F.: Quantum chemical insights into the atmospheric
718 reactions of CH2FCH2OH with OH radical, fate of $CH_2FC•HOH$ radical and ozone formation potential, Atmos. Environ., 249,
719 118247, https://doi.org/10.1016/j.atmosenv.2021.118247, 2021.
720 Lin, H., Jacob, D. J., Lundgren, E. W., Sulprizio, M. P., Keller, C. A., Fritz, T. M., Eastham, S. D., Emmons, L. K., Campbell,
721 P. C., Baker, B., Saylor, R. D., and Montuoro, R.: Harmonized Emissions Component (HEMCO) 3.0 as a versatile emissions
722 component for atmospheric models: application in the GEOS-Chem, NASA GEOS, WRF-GC, CESM2, NOAA GEFS-Aerosol,
723 and NOAA UFS models, Geosci. Model Dev., 14, 5487-5506, https://doi.org/10.5194/gmd-14-5487-2021, 2021.
724 Liu, Q., Gao, Y., Huang, W., Ling, Z., Wang, Z., and Wang, X.: Carbonyl compounds in the atmosphere: A review of abundance,
725 source and their contributions to O_3 and SOA formation, Atmos. Res., 274, 106184,
726 https://doi.org/10.1016/j.atmosres.2022.106184, 2022.
727 Liu, S., Chen, Y., Jiang, H., Shi, J., Ding, H., Yang, X., and Dong, W.: Reaction between Criegee Intermediate CH_2OO and
728 Isobutyraldehyde: Kinetics and Atmospheric Implications, ChemistrySelect, 8, e202303129,
729 https://doi.org/10.1002/slct.202303129, 2023.
730 Liu, Y., Zhou, X., Chen, Y., Chen, M., Xiao, C., Dong, W., and Yang, X.: Temperature- and pressure-dependent rate coefficient
731 measurement for the reaction of CH2OO with CH_3CH_2CHO, Phys. Chem. Chem. Phys., 22, 25869-25875,
732 https://doi.org/10.1039/D0CP04316H, 2020.
733 Long, B., Bao, J. L., and Truhlar, D. G.: Atmospheric Chemistry of Criegee Intermediates: Unimolecular Reactions and
734 Reactions with Water, J. Am. Chem. Soc., 138, 14409-14422, https://doi.org/10.1021/jacs.6b08655, 2016.

Long, B., Bao, J. L., and Truhlar, D. G.: Kinetics of the Strongly Correlated $CH_3O + O_2$ Reaction: The Importance of Quadruple Excitations in Atmospheric and Combustion Chemistry, J. Am. Chem. Soc., 141, 611-617, https://doi.org/10.1021/jacs.8b11766, 2019.

Long, B., Xia, Y., and Truhlar, D. G.: Quantitative Kinetics of HO_2 Reactions with Aldehydes in the Atmosphere: High-Order Dynamic Correlation, Anharmonicity, and Falloff Effects Are All Important, J. Am. Chem. Soc., 144, 19910-19920, https://doi.org/10.1021/jacs.2c07994, 2022.

Long, B., Xie, C., and Truhlar, D. G.: Criegee Intermediates Compete Well with OH as a Cleaning Agent for Atmospheric Amides, J. Am. Chem. Soc., 147, 22237-22244, https://doi.org/10.1021/jacs.5c07439, 2025.

Long, B., Xia, Y., Zhang, Y.-Q., and Truhlar, D. G.: Kinetics of Sulfur Trioxide Reaction with Water Vapor to Form Atmospheric Sulfuric Acid, J. Am. Chem. Soc., 145, 19866-19876, https://doi.org/10.1021/jacs.3c06032, 2023.

Long, B., Zhang, Y.-Q., Xie, C.-L., Tan, X.-F., and Truhlar, D. G.: Reaction of Carbonyl Oxide with Hydroperoxymethyl Thioformate: Quantitative Kinetics and Atmospheric Implications, Research, 7, 0525, https://doi.org/10.34133/research.0525, 2024.

Long, B., Wang, Y., Xia, Y., He, X., Bao, J. L., and Truhlar, D. G.: Atmospheric Kinetics: Bimolecular Reactions of Carbonyl Oxide by a Triple-Level Strategy, J. Am. Chem. Soc., 143, 8402-8413, https://doi.org/10.1021/jacs.1c02029, 2021.

Luecken, D. J., Hutzell, W. T., Strum, M. L., and Pouliot, G. A.: Regional sources of atmospheric formaldehyde and acetaldehyde, and implications for atmospheric modeling, Atmos. Environ., 47, 477-490, https://doi.org/10.1016/j.atmosenv.2011.10.005, 2012.

Luo, P.-L., Chen, I. Y., Khan, M. A. H., and Shallcross, D. E.: Direct gas-phase formation of formic acid through reaction of Criegee intermediates with formaldehyde, Commun. Chem., 6, 130, https://doi.org/10.1038/s42004-023-00933-2, 2023.

Lynch, B. J., Zhao, Y., and Truhlar, D. G.: Effectiveness of Diffuse Basis Functions for Calculating Relative Energies by Density Functional Theory, J. Phys. Chem. A, 107, 1384-1388, https://doi.org/10.1021/jp021590l, 2003.

Manonmani, G., Sandhiya, L., and Senthilkumar, K.: Reaction of Criegee Intermediates with SO2─A Possible Route for Sulfurous Acid Formation in the Atmosphere, ACS Earth Space Chem., 7, 1890-1904, https://doi.org/10.1021/acsearthspacechem.3c00058, 2023.

Mellouki, A., Wallington, T. J., and Chen, J.: Atmospheric Chemistry of Oxygenated Volatile Organic Compounds: Impacts on Air Quality and Climate, Chem. Rev., 115, 3984-4014, https://doi.org/10.1021/cr500549n, 2015.

Novelli, A., Vereecken, L., Lelieveld, J., and Harder, H.: Direct observation of OH formation from stabilised Criegee intermediates, Phys. Chem. Chem. Phys., 16, 19941-19951, https://doi.org/10.1039/C4CP02719A, 2014.

Novelli, A., Hens, K., Tatum Ernest, C., Martinez, M., Nölscher, A. C., Sinha, V., Paasonen, P., Petäjä, T., Sipilä, M., Elste, T., Plass-Dülmer, C., Phillips, G. J., Kubistin, D., Williams, J., Vereecken, L., Lelieveld, J., and Harder, H.: Estimating the atmospheric concentration of Criegee intermediates and their possible interference in a FAGE-LIF instrument, Atmos. Chem. Phys., 17, 7807-7826, https://doi.org/10.5194/acp-17-7807-2017, 2017.

Papagni, C., Arey, J., and Atkinson, R.: Rate constants for the gas-phase reactions of a series of C3-C6 aldehydes with OH and NO_3 radicals, Int. J. Chem. Kinet., 32, 79-84, https://doi.org/10.1002/(SICI)1097-4601(2000)32:2<79::AID-KIN2>3.0.CO;2-A, 2000.

Parker, T. M., Burns, L. A., Parrish, R. M., Ryno, A. G., and Sherrill, C. D.: Levels of symmetry adapted perturbation theory

(SAPT). I. Efficiency and performance for interaction energies, J. Chem. Phys., 140, 094106, https://doi.org/10.1063/1.4867135, 2014.
Parrish, D. D., Ryerson, T. B., Mellqvist, J., Johansson, J., Fried, A., Richter, D., Walega, J. G., Washenfelder, R. A., de Gouw, J. A., Peischl, J., Aikin, K. C., McKeen, S. A., Frost, G. J., Fehsenfeld, F. C., and Herndon, S. C.: Primary and secondary sources of formaldehyde in urban atmospheres: Houston Texas region, Atmos. Chem. Phys., 12, 3273-3288, https://doi.org/10.5194/acp-12-3273-2012, 2012.
Peltola, J., Seal, P., Inkilä, A., and Eskola, A.: Time-resolved, broadband UV-absorption spectrometry measurements of Criegee intermediate kinetics using a new photolytic precursor: unimolecular decomposition of CH_2OO and its reaction with formic acid, Phys. Chem. Chem. Phys., 22, 11797-11808, https://doi.org/10.1039/D0CP00302F, 2020.
Percival, C. J., Welz, O., Eskola, A. J., Savee, J. D., Osborn, D. L., Topping, D. O., Lowe, D., Utembe, S. R., Bacak, A., M c Figgans, G., Cooke, M. C., Xiao, P., Archibald, A. T., Jenkin, M. E., Derwent, R. G., Riipinen, I., Mok, D. W. K., Lee, E. P. F., Dyke, J. M., Taatjes, C. A., and Shallcross, D. E.: Regional and global impacts of Criegee intermediates on atmospheric sulphuric acid concentrations and first steps of aerosol formation, Faraday Discuss., 165, 45-73, https://doi.org/10.1039/C3FD00048F, 2013.
Peverati, R. and Truhlar, D. G.: M11-L: A Local Density Functional That Provides Improved Accuracy for Electronic Structure Calculations in Chemistry and Physics, J. Phys. Chem. Lett., 3, 117-124, https://doi.org/10.1021/jz201525m, 2012.
Raghunath, P., Lee, Y.-P., and Lin, M. C.: Computational Chemical Kinetics for the Reaction of Criegee Intermediate CH_2OO with HNO_3 and Its Catalytic Conversion to OH and HCO, J. Phys. Chem. A, 121, 3871-3878, https://doi.org/10.1021/acs.jpca.7b02196, 2017.
Ren, X., Harder, H., Martinez, M., Lesher, R. L., Oliger, A., Shirley, T., Adams, J., Simpas, J. B., and Brune, W. H.: HOx concentrations and OH reactivity observations in New York City during PMTACS-NY2001, Atmos. Environ., 37, 3627-3637, https://doi.org/10.1016/S1352-2310(03)00460-6, 2003.
Scollard, D. J., Treacy, J. J., Sidebottom, H. W., Balestra-Garcia, C., Laverdet, G., LeBras, G., MacLeod, H., and Teton, S.: Rate constants for the reactions of hydroxyl radicals and chlorine atoms with halogenated aldehydes, J. Phys. Chem., 97, 4683-4688, https://doi.org/10.1021/j100120a021, 1993.
Sellevåg, S. R., Stenstrøm, Y., Helgaker, T., and Nielsen, C. J.: Atmospheric Chemistry of CHF_2CHO: Study of the IR and UV−Vis Absorption Cross Sections, Photolysis, and OH-, Cl-, and NO3-Initiated Oxidation, J. Phys. Chem. A, 109, 3652-3662, https://doi.org/10.1021/jp050313m, 2005.
Sivakumaran, V., Hölscher, D., Dillon, T. J., and Crowley, J. N.: Reaction between OH and HCHO: temperature dependent rate coefficients (202–399 K) and product pathways (298 K), Phys. Chem. Chem. Phys., 5, 4821-4827, https://doi.org/10.1039/B306859E, 2003.
Stone, D., Whalley, L. K., and Heard, D. E.: Tropospheric OH and HO_2 radicals: field measurements and model comparisons, Chem. Soc. Rev., 41, 6348-6404, https://doi.org/10.1039/C2CS35140D, 2012.
Stone, D., Blitz, M., Daubney, L., Howes, N. U. M., and Seakins, P.: Kinetics of CH_2OO reactions with SO_2, NO_2, NO, H_2O and CH_3CHO as a function of pressure, Phys. Chem. Chem. Phys., 16, 1139-1149, https://doi.org/10.1039/C3CP54391A, 2014.
Sun, Y., Long, B., and Truhlar, D. G.: Unimolecular Reactions of E-Glycolaldehyde Oxide and Its Reactions with One and Two Water Molecules, Research, 6, 0143, https://doi.org/10.34133/research.0143, 2024.

Taatjes, C. A., Welz, O., Eskola, A. J., Savee, J. D., Osborn, D. L., Lee, E. P. F., Dyke, J. M., Mok, D. W. K., Shallcross, D. E., and Percival, C. J.: Direct measurement of Criegee intermediate (CH_2OO) reactions with acetone, acetaldehyde, and hexafluoroacetone, Phys. Chem. Chem. Phys., 14, 10391-10400, https://doi.org/10.1039/C2CP40294G, 2012.

Tereszchuk, K. A. and Bernath, P. F.: Infrared absorption cross-sections for acetaldehyde (CH_3CHO) in the 3μm region, J. Quant. Spectrosc. Radiat. Transfer, 112, 990-993, https://doi.org/10.1016/j.jqsrt.2010.12.003, 2011.

Thévenet, R., Mellouki, A., and Le Bras, G.: Kinetics of OH and Cl reactions with a series of aldehydes, Int. J. Chem. Kinet., 32, 676-685, https://doi.org/10.1002/1097-4601(2000)32:11<676::AID-KIN3>3.0.CO;2-V, 2000.

Wang, P.-B., Truhlar, D. G., Xia, Y., and Long, B.: Temperature-dependent kinetics of the atmospheric reaction between CH2OO and acetone, Phys. Chem. Chem. Phys., 24, 13066-13073, https://doi.org/10.1039/D2CP01118B, 2022.

Wei, Y., Zhang, Q., Huo, X., Wang, W., and Wang, Q.: The reaction of Criegee intermediates with formamide and its implication to atmospheric aerosols, Chemosphere, 296, 133717, https://doi.org/10.1016/j.chemosphere.2022.133717, 2022.

Wenger, J. C.: Chamber Studies on the Photolysis of Aldehydes Environmental, Environmental Simulation Chambers: Application to Atmospheric Chemical Processes, Dordrecht, pp, 111-119, 2006.

Werner, H.-J., Knowles, P. J., Knizia, G., Manby, F. R., Schütz, M., Celani, P., Györffy, W., Kats, D., Korona, T., Lindh, R., Mitrushenkov, A., Rauhut, G., Shamasundar, K. R., Adler, T. B., Amos, R. D., Bennie, S. J., Bernhardsson, A., Berning, A., Cooper, D. L., Deegan, M. J. O., Dobbyn, A. J., Eckert, F., Goll, E., Hampel, C., Hesselmann, A., Hetzer, G., Hrenar, T., Jansen, G., Köppl, C., Lee, S. J. R., Liu, Y., Lloyd, A. W., Ma, Q., Mata, R. A., May, A. J., McNicholas, S. J., Meyer, W., Miller III, T. F., Mura, M. E., Nicklass, A., O'Neill, D. P., Palmieri, P., Peng, D., Pflüger, K., Pitzer, R., Reiher, M., Shiozaki, T., Stoll, H., Stone, A. J., Tarroni, R., Thorsteinsson, T., Wang, M., and Welborn, M.: MOLPRO, version 2019.2, a package of ab initio programs, https://www.molpro.net/ (last access: 17 October 2025), 2019.

Xia, Y., Long, B., Liu, A., and Truhlar, D. G.: Reactions with Criegee intermediates are the dominant gas-phase sink for formyl fluoride in the atmosphere, Fundam. Res., 4, 1216-1224, https://doi.org/10.1016/j.fmre.2023.02.012, 2024.

Xia, Y., Zhang, W., Tang, X., and Long, B.: Quantitative Kinetics of the Hydrogen Shift Reaction of Methylthiomethyl Peroxy Radical (CH_3SCH_2OO) in the Atmosphere, J. Phys. Chem. A, 129, 2275-2285, https://doi.org/10.1021/acs.jpca.4c06818, 2025.

Xia, Y., Long, B., Lin, S., Teng, C., Bao, J. L., and Truhlar, D. G.: Large Pressure Effects Caused by Internal Rotation in the s-cis-syn-Acrolein Stabilized Criegee Intermediate at Tropospheric Temperature and Pressure, J. Am. Chem. Soc., 144, 4828-4838, https://doi.org/10.1021/jacs.1c12324, 2022.

Yang, X., Xue, L., Wang, T., Wang, X., Gao, J., Lee, S., Blake, D. R., Chai, F., and Wang, W.: Observations and Explicit Modeling of Summertime Carbonyl Formation in Beijing: Identification of Key Precursor Species and Their Impact on Atmospheric Oxidation Chemistry, J. Geophys. Res.: Atmos., 123, 1426-1440, https://doi.org/10.1002/2017JD027403, 2018.

Zhang, L., Truhlar, D. G., and Sun, S.: Association of Cl with C2H2 by unified variable-reaction-coordinate and reaction-path variational transition-state theory, Proc. Natl Acad. Sci., 117, 5610-5616, https://doi.org/10.1073/pnas.1920018117, 2020.

Zhang, R. M., Xu, X., and Truhlar, D. G.: TUMME: Tsinghua University Minnesota Master Equation program, Comput. Phys. Commun., 270, 108140, https://doi.org/10.1016/j.cpc.2021.108140, 2022.

Zhang, T., Wen, M., Ding, C., Zhang, Y., Ma, X., Wang, Z., Lily, M., Liu, J., and Wang, R.: Multiple evaluations of atmospheric behavior between Criegee intermediates and HCHO: Gas-phase and air-water interface reaction, J. Environ. Sci., 127, 308-319, https://doi.org/10.1016/j.jes.2022.06.004, 2023.

Zhang, Y., Mu, Y., Liu, J., and Mellouki, A.: Levels, sources and health risks of carbonyls and BTEX in the ambient air of Beijing, China, J. Environ. Sci., 24, 124-130, https://doi.org/10.1016/S1001-0742(11)60735-3, 2012.

Zhao, M., Shen, H., Zhang, J., Liu, Y., Sun, Y., Wang, X., Dong, C., Zhu, Y., Li, H., Shan, Y., Mu, J., Zhong, X., Tang, J., Guo, M., Wang, W., and Xue, L.: Carbonyl Compounds Regulate Atmospheric Oxidation Capacity and Particulate Sulfur Chemistry in the Coastal Atmosphere, Environ. Sci. Technol., 58, 17334-17343, https://doi.org/10.1021/acs.est.4c03947, 2024.

Zheng, J. and Truhlar, D. G.: Multi-path variational transition state theory for chemical reaction rates of complex polyatomic species: ethanol + OH reactions, Faraday Discuss., 157, 59-88, https://doi.org/10.1039/C2FD20012K, 2012.

Zheng, J., Zhang, S., and Truhlar, D. G.: Density Functional Study of Methyl Radical Association Kinetics, J. Phys. Chem. A, 112, 11509-11513, https://doi.org/10.1021/jp806617m, 2008.

Zheng, J., Mielke, S. L., Clarkson, K. L., and Truhlar, D. G.: MSTor: A program for calculating partition functions, free energies, enthalpies, entropies, and heat capacities of complex molecules including torsional anharmonicity, Comput. Phys. Commun., 183, 1803-1812, https://doi.org/10.1016/j.cpc.2012.03.007, 2012.

Zheng, J., Bao, J. L., Meana-Pañeda, R., Zhang, S., J.Lynch, B., Corchado, J. C., Chuang, Y., Fast, P. L., Hu, W.-P., Liu, Y.-P., Lynch, G. C., Nguyen, K. A., Jackels, C. F., Ramos, A. F., Elling son, B. A., Melissas, V. S., Villà, J., Rossi, I., Coitiño, E. L., Pu, J., Albu, T. V., Ratkiewicz, A., Steckler, R., Garrett, B. C., Isaacson, A. D., and Truhlar, D. G.: Polyrate-version 2017-C; University of Minnesota: Minneapolis, 2017.

Zheng, J., Bao, J. L., Zhang, S., Corchado, J. C., Chuang, Y., Ellingson, B. A., and Truhlar, D. G.: Gaussrate, version 2017-B; University of Minnesota: Minneapolis, MN, https://comp.chem.umn.edu/polyrate/ (last access: 17 October 2025), 2018.

Zhu, L., Talukdar, R. K., Burkholder, J. B., and Ravishankara, A. R.: Rate coefficients for the OH + acetaldehyde (CH_3CHO) reaction between 204 and 373 K, Int. J. Chem. Kinet., 40, 635-646, https://doi.org/10.1002/kin.20346, 2008.